Applied Surface Science Advances 32 (2026) 100950

Contents lists available at ScienceDirect

Applied Surface Science Advances

journal homepage: www.sciencedirect.com/journal/applied-surface-science-advances

Full Length Article

Advanced anodic molybdenum-oxide nanomaterials derived from Mo-Nb alloys

Alexander Mozalev [a,*], Maria Bendova [a], Jan Prasek [a,b], Lukas Kalina [c], Petr Smisitel [a], Francesc Gispert-Guirado [d], Eduard Llobet [e]

[a] Department of Microelectronics, Faculty of Electrical Engineering and Communication, Brno University of Technology, Technicka 10, 616 00 Brno, Czech Republic
[b] CEITEC – Central European Institute of Technology, Brno University of Technology, Purkynova 123, 61 200 Brno, Czech Republic
[c] Institute of Materials Science, Faculty of Chemistry, Brno University of Technology, Purkynova 118, 612 00 Brno, Czech Republic
[d] SRCiT, University Rovira i Virgili, Av. Paisos Catalans 26, 43007 Tarragona, Catalonia, Spain
[e] MINOS, University Rovira i Virgili, Av. Paisos Catalans 26, 43007 Tarragona, Catalonia, Spain

ARTICLE INFO

Keywords:
Anodizing
Molybdenum oxide
Porous anodic alumina
Semiconductor
Pseudocapacitance
Gas sensing
X-ray photoelectron spectroscopy

ABSTRACT

The fabrication of inorganic semiconducting nanomaterials with a high content of molybdenum oxide (MoO_x), self-organized in arrays on a substrate, has long been a challenge, limiting the utilization of MoO_x nanostructures in on-chip micro- and nanodevices. Here, for the first time, arrays of MoO_x nanostructures, such as bulges, columns, and rods, of high densities ($10^8 - 10^{10}$ cm^{-2}), self-standing on a substrate, are synthesized via the in situ anodization of sputter-deposited Mo-Nb alloy layers with variable Mo content, ranging from 5 to 95 at. %, covered with a thin Al layer. The approach involves the growth of a porous anodic alumina (PAA) film that enables the formation of fully amorphous molybdenum-niobium mixed-oxide nanostructures within and under the PAA nanopores. By combining SEM, XPS, and XRD analyses, it is shown that, after selective PAA dissolution, the free-standing nanostructures are composed of a dominating amount of MoO_x with various Mo^{n+} cations (n = 6 to 3) mixed at the atomic level with a minor amount of Nb_2O_5 and NbO_2 suboxide, which are 'doped' at the surface with Al_2O_3 originating from the PAA cell walls and 'serving' as a shape stabilizer. The record-high Mo content achieved with this technology is 92 at. %. The accomplishment is due to the enhanced migration of Mo^{n+} cations within the mixed oxide inside the PAA nanopores and along the pore walls. Annealing at 550°C induces a unique phase separation, resulting in MoO_2 nanocrystals dispersed within the amorphous MoO_x-Nb_2O_5 matrix and an increased oxidation state of MoO_x at the film surface. The cyclic voltammetry and electrochemical impedance spectroscopy examinations confirm that the entire surface of the oxide nanorods is an n-type semiconductor with a charge carrier density of 2×10^{21} cm^{-3}. The highly competitive pseudocapacitive properties of the nanoarray derived from Mo-19at. %Nb alloy are disclosed, yielding a capacitance of ~10 mF cm^{-2}, rendering the film promising as a 3D semiconductor nanoelectrode for emerging on-chip energy-storage microdevices. Moreover, the film efficiently serves as a gas-sensing layer for rapidly and selectively detecting low concentrations of C_2H_5OH (10 ppm) and CO (100 ppm). More potential applications include antibacterial coatings, self-cleaning surfaces, and electrochromic films, where the rod-like nanomorphology and the large number of Mo-containing reactive sites are highly desirable.

1. Introduction

Molybdenum oxides (MoO_x) are versatile oxide compounds with diverse potential applications as functional materials in electronic passives, catalysts, gas sensors, field emitters, superconductors, thermal materials, electrochromic coatings, electrochemical energy-storage devices, or supersurfaces [1–8]. The family of molybdenum oxides is a large group of materials united by their ability to possess various crystal structures, oxidation states, and mixed-valency oxides [9,10]. MoO_x may be stoichiometric MoO_3, which features a wide bandgap of >2.7 eV, semiconducting MoO_{3-x} ($0 < x < 1$), and eventually semimetallic MoO_2 with a significantly reduced bandgap. The lowest-valency cubic MoO,

* Corresponding author.
E-mail addresses: mozalev@vutbr.cz (A. Mozalev), bendova@vutbr.cz (M. Bendova), prasek@vutbr.cz (J. Prasek), kalina@fch.vut.cz (L. Kalina), smisitel@vutbr.cz (P. Smisitel), francesc.gispert@urv.cat (F. Gispert-Guirado), eduard.llobet@urv.cat (E. Llobet).

https://doi.org/10.1016/j.apsadv.2026.100950
Received 7 January 2026; Received in revised form 3 February 2026; Accepted 7 February 2026
Available online 24 February 2026
2666-5239/© 2026 The Authors. Published by Elsevier B.V. This is an open access article under the CC BY license (http://creativecommons.org/licenses/by/4.0/).

Mo_2O, and Mo_3O phases exhibit excellent metallic conductance [2,11, 12].

Various nanostructuring techniques have been employed to enhance the functional properties of MoO_x, which are associated with substantially increasing the surface-to-volume ratio and shortening the carrier transport pathways compared to bulk or thin-film oxides [2,9]. Moreover, doping or mixing MoO_x with similar or dissimilar oxides has been tried to enhance or modify the properties of the individual oxides, although such techniques typically require extreme temperatures, high-vacuum conditions, and tall-budget equipment [13]. Even though nanosized MoO_x-based dots, wires, tubes, flowers, platelets, spheres, or belts in solution or randomly dispersed on substrates have been reported [2,6], the formation of ordered arrays of 1-D MoO_x-based nanomaterials, amorphous or crystalline, spatially separated, vertically protruding from and self-aligned on substrates has long been a challenge due to the difficulties in precisely controlling the formation conditions, size, morphology, chemistry, crystallography, and locations of individual nano-elements on the substrates [1,9]. The localized charge-carrier transport within individual 1D current passways, such as MoO_x semiconductor nanowires or nanorods arranged in 3D nanoarrays on substrates, complemented by the enhanced surface reactivity, would be a stepping stone toward emergent MoO_x-based on-chip electronic, optoelectronic, catalytic, or energy-storage nanodevices [7,14].

As a step forward, we have recently proposed a method based on the nanoelectrochemical fabrication principles [15] to synthesize MoO_x-based 'nanocables' that are vertically aligned on a substrate via self-organized anodizing of sputter-deposited Al/Nb/Mo laminates [16]. The method involved the growth of a porous anodic alumina (PAA) film [15,17], followed by in-situ PAA-assisted anodization [18,19] of the underlying Mo *through the thin Nb interlayer*. The developed technique enabled the sustainable growth of amorphous MoO_x nanorods within the PAA nanopores in several aqueous electrolytes, a feat that had not been possible with any other reported methods, including electrochemistry. Although the rods' cores were a highly-doped *n*-type semiconductor showing competitive pseudocapacitive behavior, the major drawback was the low Mo content (< ~20 at. %) in the rods' shells. This rendered the shells nearly dielectric, excluding their contribution to complex charge carrier transport and surface reactions, thus limiting their application potential.

From the above consideration, it is of vast importance to find the ways to enlarge the molybdenum content in the nanorods substantially, avoid the formation of core/shell contrasting properties by making the oxide composition more homogeneous, and significantly enhance the surface reactivity and semiconducting properties of the rods, such that the entire film surface can contribute to increasing the electron transport and enhancing the redox reactions, facilitating the application of such advanced nanomaterials for pseudocapacitors, chemical sensors, catalysts, photo- and electrochromics, or hydrogen generators.

In the present work, we developed highly challenging nanoelectrochemical fabrication processes based on in-situ PAA-assisted anodizing of *Mo-Nb binary alloys* with variable Mo content reaching 95 at. %, prepared by co-sputtering deposition of Mo and Nb metals on solid substrates. Nanostructured anodic oxide films synthesized via the PAA-assisted anodizing of various Mo-Nb alloys were examined using high-resolution scanning electron microscopy (SEM), X-ray photoelectron spectroscopy (XPS), X-ray diffraction (XRD), electrochemical impedance spectroscopy (EIS), and Mott-Schottky analysis. From a fundamental science viewpoint, the in situ anodizing of a Mo-Nb solid solution through the PAA nanopores opens a unique possibility to investigate cooperative ionic transport, solid-state reactions, and oxide dissolution in self-supported MoO_x nanostructures mixed with other metal oxides under a high electric field. The functional properties that determine the application potential of the nanoarrays were explored using cyclic voltammetry (CV) in solution and by performing gas-sensing tests using a metal/semiconductor microchip with the MoO_x nanoarray serving as the active layer.

2. Experimental section

2.1. Sample preparation

Face-side polished Si wafers (*n*-type, 4", 500 μm thick, 40 Ω cm), covered with a 300 nm thick SiO_2, were used as starting substrates. Layers of Mo-Nb alloys, 170 nm thick, were deposited via magnetron co-sputtering of Mo (99.95 %) and Nb (99.95 %) targets, step-wise covering a range of Mo concentrations in the alloys from 10 to 95 atomic percent. After a 30-minute break to cool the wafers, layers of Al, 700 nm thick, were deposited by magnetron sputtering of an Al (99.999 %) target. All the targets utilized in this work were from Kurt J. Lesker Company GmbH.

The setup used for anodizing and re-anodizing experiments with individual pieces cut from the wafers was described in previous publications [20]. Depending on the current density range, either an Agilent 5752A or a Keithley 2410 programmable power supply, controlled by a homemade software written in LabVIEW, was used as the anodizing unit. Typically, anodizing was carried out to convert the upper Al layer into a PAA film, which was followed by re-anodizing of the underlying Mo-Nb alloy to a higher voltage through the PAA overlayer, striving to achieve the growth of mixed anodic oxides within the pores. Aqueous solutions of sulfuric (H_2SO_4), oxalic ($H_2C_2O_4$), phosphoric (H_3PO_4), malonic [$CH_2(COOH)_2$] [21], tartaric [$(CH(OH)(COOH))_2$] [22], etidronic [$CH_3C(OH)(PO_3H_2)_2$] [23], and citric ($C_6H_8O_7$) [24] acids were tested as the anodizing and re-anodizing electrolytes. Anodizing and re-anodizing processes were carried out under constant-current polarization, followed by a voltage hold to ensure uniform anodic oxide growth across the sample surface. The PAA overlayers were dissolved, fully or partially, in a 'selective etchant', which was prepared and used as described elsewhere [25,26]. Finally, the samples were rinsed in ultrapure deionized water and dried in air at 120°C for 15 minutes. Selected samples were annealed at 550°C for 3 hours either in ambient air at atmospheric pressure (hereafter the '*air-annealed*' samples) or at a residual pressure of 10^{-5} Pa (hereafter the '*vacuum-annealed*' samples).

2.2. Analysis and measurements

Scanning electron microscopy (SEM) observations of surfaces and cross-sections of the anodic films before and after the PAA dissolution were performed in a TESCAN MIRA II field-emission instrument operated at 30 kV accelerating voltage. Due to the in-beam detector for secondary electrons, no conducting layers were required over the sample surfaces to reduce the charging effect before observation. For statistical analysis, the surface SEM images were analyzed using ImageJ software.

X-ray photoelectron spectroscopy (XPS) analysis was conducted using a Kratos Axis Ultra DLD spectrometer (monochromatic Al Kα source) with X-ray emission power of 75 W and typical operating pressures of less than 1.3×10^{-9} mbar. The X-ray beam was focused to a 300 μm × 700 μm spot. The emitted electrons were detected at fixed pass energies of 160 eV for the survey spectra and 20 eV for the high-resolution spectra. The Kratos charge neutralizer system was employed in all measurements. CasaXPS version 2.3.17 was used for spectra analysis. GL(30) profiles were selected for all components except the metallic core lines of Mo 3d and Nb 3d and the contributions of crystalline MoO_2 (see ESI). All spectra were charge-corrected to give the adventitious C 1s spectral component (C−C, C−H) binding energy of 284.8 eV. The quantitative analysis was performed on the high-resolution spectra based on the relative sensitivity factors from CasaXPS, which are suitable for Kratos Axis spectrometers and are referenced to the F 1s peak. Further details are described elsewhere and in the ESI [27,28].

X-ray diffraction (XRD) patterns of the experimental samples were recorded using a Bruker-AXS D8-Discover diffractometer equipped with a parallel incident beam (Göbel mirror) and a vertical θ-θ goniometer,

operating at 40 kV and 40 mA to generate Cu Kα radiation. An X-ray collimator was used to analyze an area of 500 μm in reflection mode. The VÅNTEC-500 detector (silicon strip technology, active area 30 cm × 30 cm, frame size 2048 pixels × 2048 pixels) was placed at a 15 cm distance from the sample surface. For each sample, three frames were collected, covering 20–90° 2θ, and an exposure time of 600 s per frame to obtain a 2D diffractogram. This diffractogram was then γ-integrated to produce the conventional 2θ vs. intensity diffractogram. The Rietveld refinement [29] was performed using TOPAS 6.0 software (Bruker AXS GmbH, 2017) [30] with the identified crystal structures. Further details are available in the ESI.

The EIS and CV analyses were performed in a 1 M Na_2SO_4 electrolyte at 22°C using an Autolab PGSTAT204 Potentiostat/Galvanostat with a FRA32M module (Metrohm). A three-electrode setup was installed inside a cylindrical PTFE cell, securing a circular area of 0.08 cm^2 on the sample surface [16]. The sample was the working electrode, an Au plate was the counter electrode, and an Ag/AgCl (1 M KCl) was the reference electrode. The CVs were typically recorded between −1.2 and 0.0 V *vs.* Ag/AgCl at a scan rate of 20 mV s^{-1}, starting from the open circuit potential (OCP) in the anodic direction toward the highest potential, followed by a set of cathodic and anodic sweeps, and finishing near the initial OCP value. EIS was performed by applying a sinusoidal perturbation of 10 mV to the OCP or selected bias voltages (Mott--Schottky measurements) in a frequency range of 1 MHz to 0.01 or 0.1 Hz. During the Mott-Schottky measurements, a 3-minute potential hold was applied at each point before the EIS, and the current was recorded. The EIS data were analyzed using computer simulation and fitting software Autolab NOVA (version 1.10). The entire frequency range was used for fitting with an equivalent electrical circuit containing a constant phase element (CPE) in parallel with a resistor, from which the capacitances were extracted as $C = Y_0^{1/n} R_p^{(1-n)/n}$ [31]. Unless stated otherwise, the measured and calculated parameters were referenced to the apparent surface area exposed to the electrolyte.

Gas sensing tests were performed in a custom-made chamber (125 ml) under a constant gas flow of 200 sccm. The desired concentrations of gases were obtained by mixing pure synthetic air (20 % O_2 and 80 % N_2, Linde Gas) with calibrated gas (either 100 ppm ethanol or 1000 ppm CO, all in synthetic air), using mass-flow controllers. Parallel metal strips, 3 mm x 0.5 mm in size, separated by a distance of 1.0 mm, were formed via thermal evaporation of 200 nm NiCr through shadow masks on the surface of the nanostructured film synthesized in a sulfuric acid electrolyte and annealed in air, to serve as conducting electrodes. The resistance between the electrodes was measured in the presence of dry synthetic air or diluted gas using a Keithley 2410 Source Meter, controlled by LabVIEW software via a PC. The chamber was equipped with a miniaturized, flexible probe system installed above a heated platform capable of reaching temperatures of up to 300°C, designed for measuring sensor chips without the need for bonding or packaging. The normalized sensor response, S, was defined as $(R_{gas}-R_0)/R_0$, where R_0 is the baseline resistance in air, and R_{gas} is the resistance in the presence of a test gas.

3. Results and discussion

3.1. Anodizing behavior

Thin-film Mo-Nb binary alloys with various Nb content covering the range from 5 to 90 at. % were prepared via the magnetron co-sputter deposition onto the wafers. For simplicity, the alloys will be coded as Mo-*x*Nb (e.g., Mo-5Nb, Mo-10Nb, etc.), where the *x*-value denotes the atomic percent of Nb, which was determined by high-resolution XPS analysis (see ESI).

Aqueous solutions of various acids, listed in the Experimental section, were tested as the electrolytes for anodizing/re-anodizing the Al/Mo-Nb bilayer samples to achieve the nucleation and solid-state growth of Mo-based anodic oxides within and under the PAA nanopores. Only 0.6 M oxalic and 0.2 M sulfuric acid (hereafter the 'OX' and 'SU' electrolytes, respectively) appeared appropriate for processing the Al/Mo-Nb bilayers with the moderate and high Mo content in the alloy. For the OX electrolyte, the upper concentration limit of Mo in the alloy appeared to be 81 at. % (Mo-19Nb), above which PAA-assisted anodizing of the alloy was impossible. However, the use of the SU electrolyte allowed the Mo concentration limit to be extended up to 95 at. %, which is a significant achievement of this work. The other acid solutions probed in this study, all of which yielded substantially higher anodizing voltages at comparable current densities, resulting in more distanced pores in the PAA, were only suitable for alloys containing less than ~60 at. % Mo. The need to decrease Mo content in the alloy to enable its PAA-assisted anodizing seems to correlate with increasing anodizing voltage associated with the following order of anodizing electrolytes: sulfuric < oxalic < malonic < phosphoric < tartaric < citric < etidronic acid, as expressed in Fig. 1. As the primary challenge was to anodize Mo-Nb alloys with as high a Mo content as possible, the focus of this study will be on the anodic films synthesized in the OX and SU electrolytes.

As a typical example, Fig. 2a shows the voltage-time and current-time responses during the anodizing of an Al/Mo-19Nb bilayer in the SU electrolyte at a constant current density of 7 mA cm^{-2}. Under the above conditions, a steady-state voltage of 25 V is established during the PAA growth, followed by a short voltage hold after the anodizing front reaches the alloy layer. The voltage transient appears typical for mild porous anodizing of aluminum in a sulfuric acid electrolyte at moderate current densities, with no abnormalities that might occur during PAA growth or at the PAA/alloy interface [32]. It is expected that the anodic oxidation of the alloy layer begins already during the voltage hold. At the commencement of constant-current re-anodizing (Fig. 2b), a short induction period is evident before the voltage begins to increase rapidly (marked with a dashed circle), reaching a value approximately equal to that established during the steady-state PAA growth. Then the voltage rise retards twice, until it becomes almost constant, reaching the set point, followed by a short voltage hold until the current drops approximately fivefold. The changes in the voltage-time slope during the voltage rise are associated with the modification and penetration of the PAA barrier layer by the oxide that grows underneath, followed by the partial field-assisted dissolution of the PAA barrier layer and further oxide growth solely within the pores.

Fig. 2c shows the voltage and current transients during anodizing the same Al/Mo-19Nb bilayer in the OX electrolyte at an optimized current density of 20 mA cm^{-2}. As noted above, the Mo-19Nb alloy has the minimal Nb concentration that has yet made possible PAA-assisted anodizing of the alloy in the OX electrolyte. A steady-state voltage of

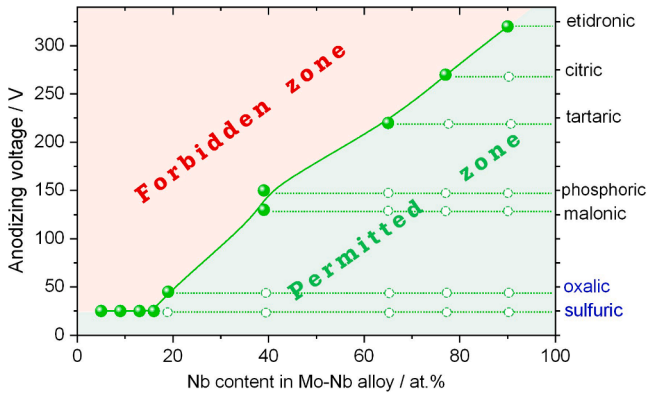


Fig. 1. Correlation of the anodizing voltage and the electrolyte composition with Nb content in Mo-Nb alloys that allow PAA-assisted anodizing. The plot shows that, with increasing Nb content in the alloy, the concentration zone that allows for PAA-assisted anodizing of Mo-Nb alloys (permitted zone) expands, involves more acids, and enables higher anodizing voltages.

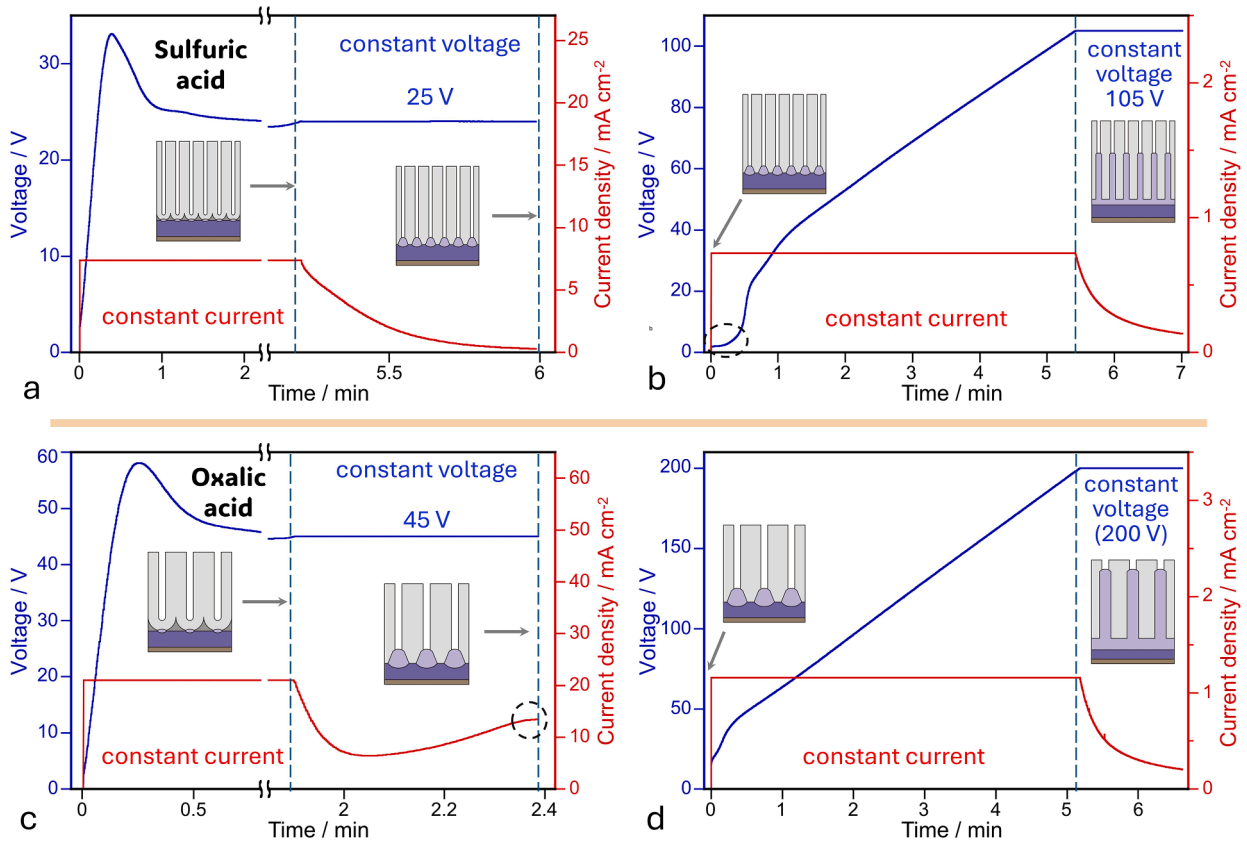


Fig. 2. The voltage-time and current-time responses from Al(800 nm)/Mo-19at.%Nb(170 nm) bilayer during (a) anodizing in 0.2 M H_2SO_4 (sulfuric acid), followed by (b) re-anodizing to 105 V and (c) anodizing in 0.6 M $H_2C_2O_4$ (oxalic acid), followed by re-anodizing to 200 V. The embedded schematics illustrate the expected cross-sectional views of the anodic films after completion of the anodizing and re-anodizing processes.

45 V is established during PAA growth, as expected at this current density [33,34]. Contrary to the SU anodizing, after a short period of current decay during the voltage hold, the current begins to rise, and once it reaches a maximum (13 mA cm^{-2}), the polarization is turned off to prevent the current from decreasing again. If the current is allowed to further decrease after reaching its maximum, it will make re-anodizing impossible, and the PAA layer may peel off. At the commencement of re-anodizing, even though the voltage does not immediately increase to the value established during steady-state PAA growth (45 V), the induction period is not observed. After reaching ~40 V, the voltage rises almost linearly until it attains the set value of 200 V in this example (Fig. 2d). More generally, the maximum re-anodizing voltage that can be attained with the PAA-assisted anodizing of Mo-Nb alloys in the OX electrolyte was as high as 400 V, substantially exceeding the limit for processing the Al/Nb/Mo trilayer reported previously (~300 V) [16]. Another feature of anodizing in this electrolyte is that if the Nb concentration in the alloy exceeds some 20 at. %, the current decays monotonically during the voltage hold, as does the anodizing current during the normal PAA-assisted anodization of pure niobium [35]. The schematics in Fig. 2 preliminarily suggest how the films may look after completing the anodizing and re-anodizing stages in the SU and OX electrolytes; these will be updated later based on the SEM observations.

Notably, a smooth anodic oxidation of the Mo-Nb alloy films without Al layers on top was impossible in any of the solutions tested in this study due to an extended induction period, which has also been reported for anodic treatment of pure Mo layers [36], accompanied by an intensive electrochemical dissolution of the alloy combined with the chemical dissolution of the oxide, which prevented the formation of stable solid-state compounds. This highlights the uniqueness of the PAA-assisted anodizing of Mo-Nb alloys for growing stable Mo-Nb anodic oxides, which cannot be accomplished by any other technique reported to date.

3.2. *Film morphology*

The anodic films derived from the PAA-assisted anodizing/re-anodizing of the Mo-19Nb alloy in the OX electrolyte were selected as representatives for SEM analysis to demonstrate the changes in the morphology with the formation stage (Fig. 3). The films anodized at 45 V are shown in the upper row, followed by re-anodizing to 220 V (middle row) and 300 V (lower row); the anodizing and re-anodizing curves are as in Fig. 2c and d. More intermediate re-anodizing steps are depicted in Fig. S1.

The cross-section of the anodized sample in Fig. 3a reveals an array of nanobulges protruding into the pores above the remaining alloy surface, resulting from the local anodic oxidation of the underlying alloy, surrounded by a continuous network of unoxidized aluminum, which remains after completing the anodizing process, as pointed out by the green arrows. An instability in anodic oxide formation is noted through the formation of protuberances over the tops of the bulges, marked with the blue arrows. Through the following re-anodizing process, the bulges transform into oxide nanorods, which lengthen within the pores in proportion to the re-anodizing voltage, without any sign of instability at the electrolyte/rod-top interfaces (Fig. 3d–i). In all cases, the measured population density of the oxide protrusions is 8×10^9 cm^{-2}, which agrees with the expected pore density in the PAA overlayer. The mean diameter of the rods is 50 nm, being independent of the reanodizing voltage, which is 1.7 times the average diameter of the PAA nanopores (29 nm). The rods are anchored to a continuous anodic-oxide layer beneath the former PAA/alloy interface (hereafter the 'bottom layer'). The rods' length and the bottom-layer's thickness increase proportionally to the re-anodizing voltage, and the oxide/alloy interface

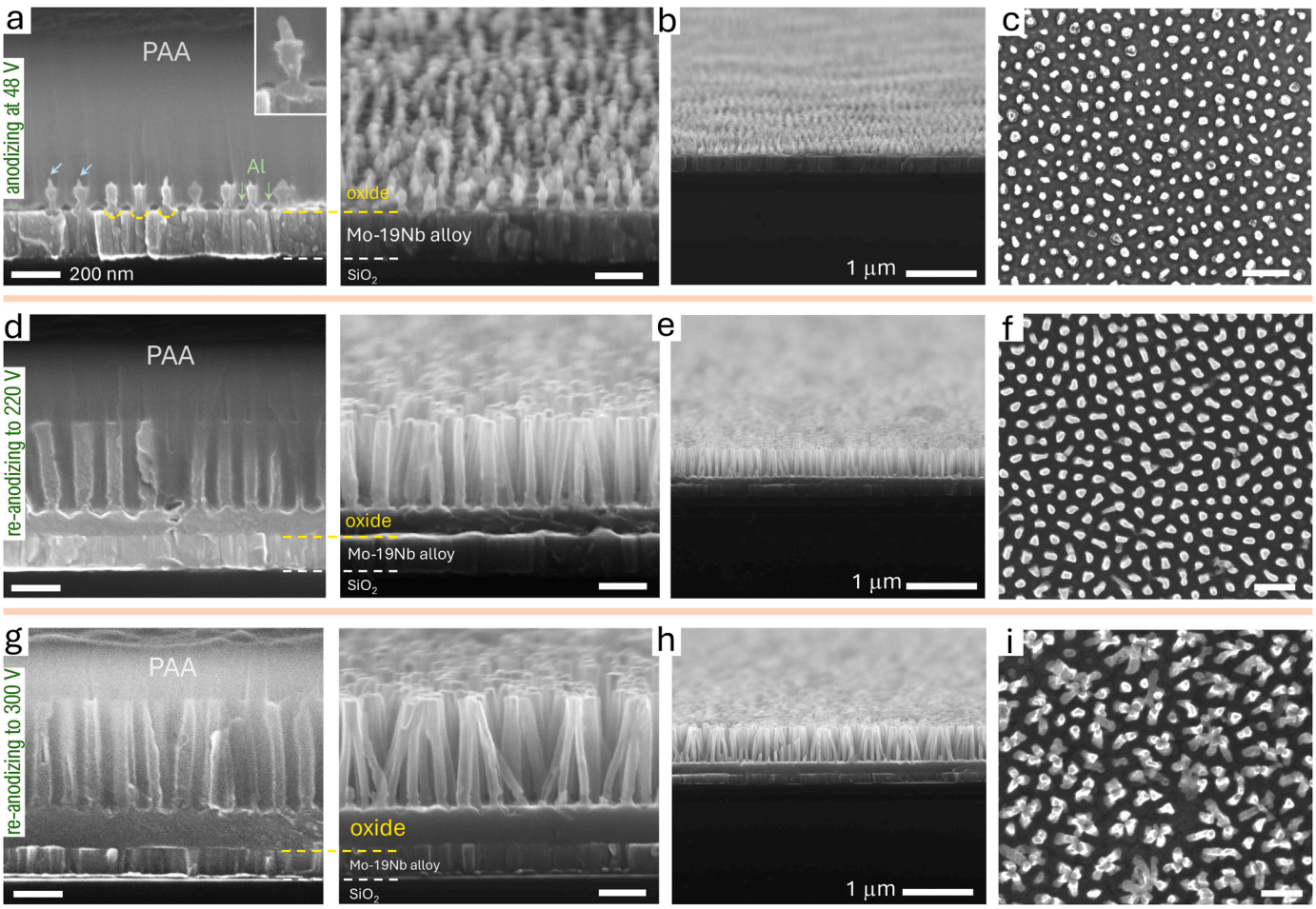


Fig. 3. Cross-sectional, 3D, and surface SEM views of anodic films synthesized from an Al/Mo-19at.%Nb bilayer (a–c) via the anodizing in 0.6 M oxalic acid at 45 V, as in Fig. 2c, followed by (d–f) re-anodizing to 220 V or (g–i) re-anodizing to 300 V. Images in (a, d, and g) show the as-prepared anodic films. Images in (b, c, e, f, h, and i) show the corresponding films after PAA dissolution. All undefined scale bars are 200 nm in length.

(yellow dashed line) appears flat already after the 220-V re-anodizing. This means that the nanosized concave-like areas of the bottom oxide, which develop during the anodizing stage (Fig. 3a, yellow dashed line), merge fully into a uniform solid layer at approximately 220 V. With the re-anodizing voltage approaching 300 V, the tops of the rods begin to agglomerate (Fig. 3h and i) due to the flexibility of the rods' roots and the increasing impact of van der Waals forces.

Fig. 4a–c shows SEM views of the anodic film derived from the PAA-assisted anodizing/re-anodizing of the same Mo-19Nb alloy in the SU electrolyte (see Fig. 2a and b). Typically, for the SU anodizing at 25 V followed by re-anodizing to 105 V, an array of tiny rod-like nano-protrusions is formed, each about 30 nm wide and 220 nm long, of the highest population density of 3×10^{10} cm^{-2}, anchored to a bottom-oxide layer. Similar to the OX case, the film thickness increases with the re-anodizing voltage. The tops of the SU rods tend to agglomerate already at about 130 V (not shown).

The extended possibilities of PAA-assisted anodizing of the Mo-Nb alloy layers are further demonstrated in the SEM views of Fig. 4d–j, depicting anodic films formed from the Mo-39Nb alloy via the PAA-assisted anodizing/re-anodizing in phosphoric (150/400 V) and malonic (135/400 V) acid electrolytes. Substantially larger sizes of the oxide protrusions and smaller population densities are noted for both cases. While the phosphoric acid-made pillars are distributed uniformly across the sample surface (Fig. 4, middle row), the malonic acid-made columns grow in domains separated by unpopulated areas of sizes comparable to the domain sizes (Fig. 4, bottom row). The domainization effect may be due to the larger difference in ionic resistance of the alumina and the anodic oxide formed on the alloy in the malonic acid electrolyte. Practically, such a domainization may help reach super-hydrophobic properties of the surfaces, which are in demand for self-cleaning applications.

Through numerous experiments and adjustments of electrical and electrolytic conditions, we successfully achieved the PAA-assisted anodizing/re-anodizing of the Mo-Nb alloys over the entire range of Mo concentrations. The results appeared to be highly dependent upon the nature and concentration of the solutions, current density, and formation voltage, as expressed in Fig. 1. In this regard, the most significant achievement was the PAA-assisted processing of the Mo-5Nb alloy, which had the highest Mo content (95 at. %), in a sulfuric acid electrolyte. This will be discussed in reference to the film's chemical composition in Section 3.3.7. We selected the nanoarrays synthesized in the OX and SU electrolytes as model systems for performing thorough chemical and structural analyses and investigating ionic transport during the growth of mixed Mo-Nb anodic oxides.

3.3. *Film composition*

The chemical composition and bonding states in the as-synthesized and annealed anodic films were investigated by XPS, a powerful tool for studying the formation of electrochemically induced dielectric and semiconducting layers [37]. Hereafter, the films obtained after dissolving the PAA layer in the selective etchant will be referred to as the 'PAA-free' samples. The films with a partially dissolved PAA layer, to expose the oxide protrusions but keep the bottom layer still covered by

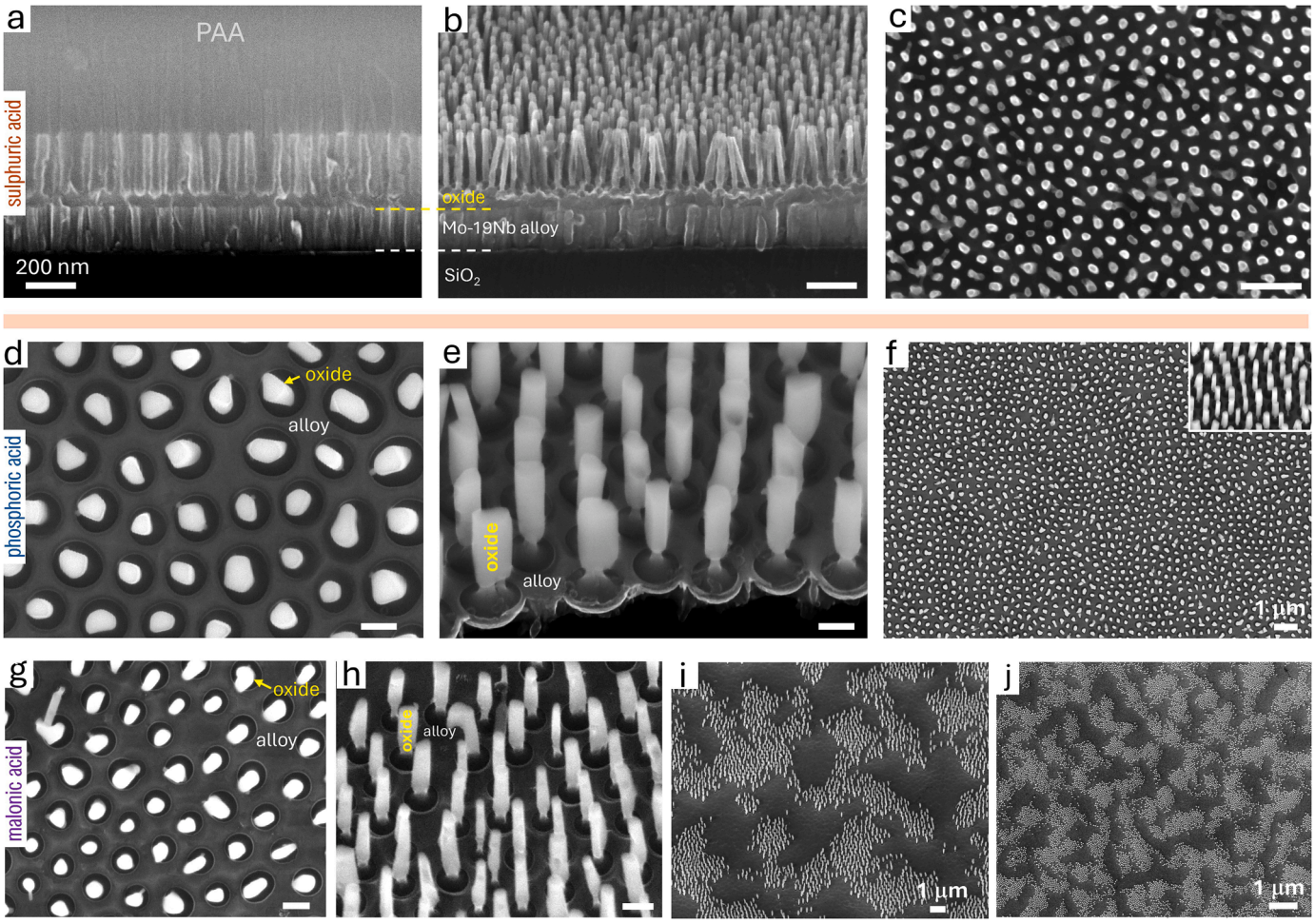


Fig. 4. Cross-sectional, 3D, and surface SEM views of anodic films synthesized from (a–c) an Al/Mo-19at.%Nb bilayer via the anodizing/re-anodizing in 0.2 M sulfuric acid at 25/105 V, as in Fig. 2a and b, (d–f) an Al/Mo-39at.%Nb bilayer via the anodizing/re-anodizing in 0.2 M H_3PO_4 (phosphoric acid) at 150/400 V, and (g–j) an Al/Mo-39at.%Nb bilayer via the anodizing/re-anodizing in 0.6 M $CH_2(COOH)_2$ (malonic acid) at 135/400 V. The images in (b–j) were recorded after the PAA had been dissolved. All undefined scale bars are 200 nm in length.

the remaining PAA, will be distinguished as the 'PAA-half-etched' samples. The re-anodized films with the unmodified PAA layer will be mentioned as the 'PAA-inbuilt' samples.

Narrow-scan C 1s, O 1s, Mo 3d, Nb 3d, Al 2p, and S 2p spectra were collected to analyze the core levels and bonding states of the elements of interest. In the following, the XPS analysis will be presented for (1) the OX anodic films derived from the Mo-19Nb alloy (Fig. 5) and partially (2) the SU anodic films derived from the Mo-5Nb alloy (Fig. 8), which reflects the highest Mo content (95 at. %) in the alloy that can be processed via PAA-assisted anodizing. The XP spectra of the as-deposited Mo-Nb alloys, various annealed anodic films, and SU films are shown in Fig. S2, S5, and S6. Additionally, a justification for the narrow-spectrum deconvolution approaches employed in this study is provided in the ESI.

3.3.1. *Molybdenum oxides*

The analysis of **Mo 3d** spectra shown in Fig. 5, 7, and 8 and Fig. S6, reveals that each anodic film is composed of Mo oxides with multiple oxidation states of Mo cations. The oxide composition may be expressed as $Mo^{VI}_{x1}Mo^{V}_{x2}Mo^{IV}_{x3}Mo^{III}_{x4}O$. The degree of MoO_3 reduction in each oxide will be distinguished by an average oxidation state (AOS) of Mo cations, with assigning MoO_x to the following characteristic types: Type I – 'highly reduced' MoO_x, AOS 4.10±0.15, typical for the PAA-free films (Fig. 5a,d and Fig. 8c); Type II – 'moderately reduced' MoO_x, AOS 4.74 ±0.15, detected in the re-anodized PAA-half-etched films (Fig. 5g and Fig. S6e); and Type III – 'slightly reduced' MoO_x, AOS 5.07±0.1, occurring in the annealed PAA-free films (Fig. 5j and Fig. S6i). Furthermore, the AOS value of Mo, as well as the Mo content, varies in the nanorods and the bottom layer.

The Mo 3d spectra in Fig. 5 appear typical for the anodic films derived from various alloys (except for the Mo-90Nb case) processed in the OX electrolyte. In the Mo 3d spectrum of the *anodized* PAA-free sample (Fig. 5a), the five doublets are assigned to Mo^{n+} cations with n = 6, 5, 4, 3, and 0. The metallic component (~3 % of all Mo species) is due to the alloy residues surrounding the bulges, whereas Mo^{n+} components are due to the MoO_x suboxides mixed in the anodic film. The AOS value (excluding the metallic contribution) is 4.18, which is typical for Type I MoO_x.

The spectrum of the *re-anodized* to 180 V PAA-free film (Fig. 5d) is composed of the same oxide components; Mo^0 is not present, however. The distribution of cations is only slightly different. The amount of Mo^{3+} is higher than that of Mo^{4+}, which is the opposite of the anodized sample. With an AOS of 4.01, the oxide is of Type I MoO_x. The absence of the Mo^0 doublet implies the full consumption of the alloy around the rod roots during re-anodizing to 180 V.

The *re-anodized PAA-half-etched* film (Fig. 5g) exhibits a substantially different Mo 3d pattern: the Mo^{6+} doublet becomes significantly more intense, reflecting a substantial increase in the AOS value (4.63), which renders the oxide Type II MoO_x. Such a difference between the PAA-free and PAA-half-etched re-anodized films (Fig. 5d and g) is explained by a

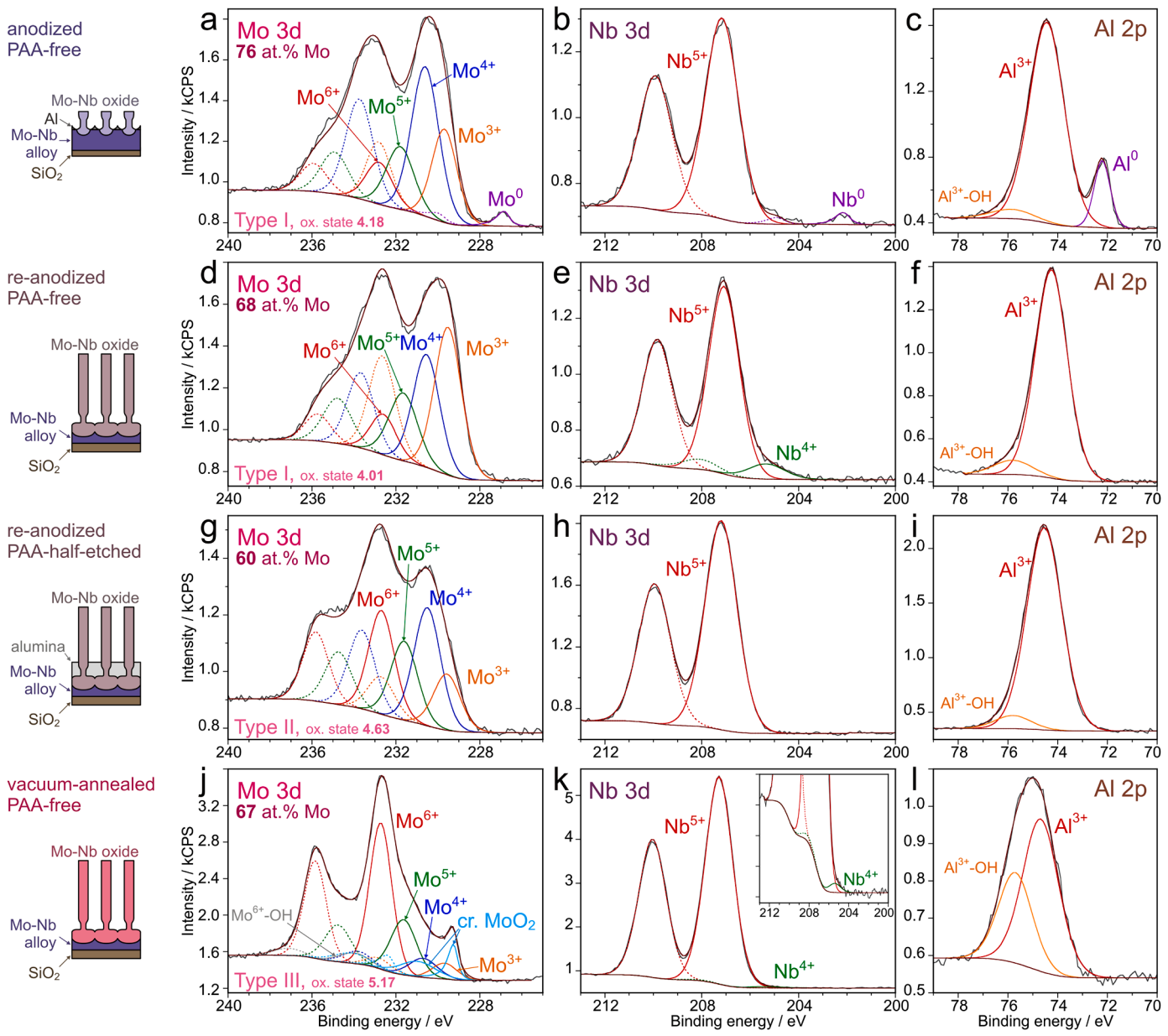


Fig. 5. Experimental and curve-fitted narrow scan (left column) Mo 3d, (middle column) Nb 3d, and (right column) Al 2p XP spectra of anodic films synthesized from an Al/Mo-19at.%Nb bilayer via (a–c) the anodizing in 0.6 M oxalic acid at 45 V as in Fig. 2c followed by PAA dissolution, (d–f) re-anodizing to 180 V followed by PAA dissolution, (g–i) re-anodizing to 180 V followed by partial PAA dissolution (PAA-half-etched film), and (j–l) re-anodizing to 180 V followed by annealing in vacuum (10^{-5} Pa) and PAA dissolution. The peak positions, FWHMs, and atomic concentrations are summarized in Table S1.

higher degree of oxide reduction in the bottom layer than in the rods' surface. Fig. 6a illustrates the trend of increasing the AOS value from the PAA-free to PAA-half-etched films synthesized from various alloys in the OX and SU electrolytes.

The only deviation from the described trend appears to be the case of Mo-90Nb alloy (see Mo 3d spectra in Fig. S4). The PAA-free film synthesized from this alloy contains Type II MoO_x (AOS 4.75) while the PAA-half-etched film contains even more oxidized Type III MoO_x with the highest AOS value of 5.48. These features, combined with the highest Nb content in the mixed oxide, may help adjust the electronic properties of PAA-assisted Nb_2O_5-based nanostructures doped with minor amounts of MoO_x for specific applications in electronics, which may be the subject of future work.

3.3.2. *Niobium oxides*

The **Nb 3d** spectra of the anodic films synthesized from the Mo-19Nb alloy in the OX electrolyte (Fig. 5b,e, and h) appeared typical for all the alloys, including the Mo-90Nb case. The surface of the anodized sample (Fig. 5b) contains a dominating amount of Nb_2O_5 and a small portion of Nb^0. The Nb° component, ~3 % of all Nb species in the spectrum, is attributed to the alloy residues surrounding the bases of the nanobulges (in agreement with the corresponding Mo 3d spectrum). The re-anodized PAA-free film (Fig. 5e) does not contain Nb^0 at the surface, because the bottom oxide fully covers the remaining alloy. However, the film contains Nb_2O_5 mixed with NbO_2; the presence of ~10 % Nb^{4+} is noted for the re-anodized films derived from various alloys, resulting in an AOS of Nb = 4.90. In contrast, the PAA-half-etched films (Fig. 5h) contain stoichiometric Nb_2O_5, without any suboxides. This means that the NbO_x suboxides reside solely in the bottom oxide layer.

3.3.3. *'Doping' with alumina*

The surface of the anodized PAA-free film synthesized from the Mo-

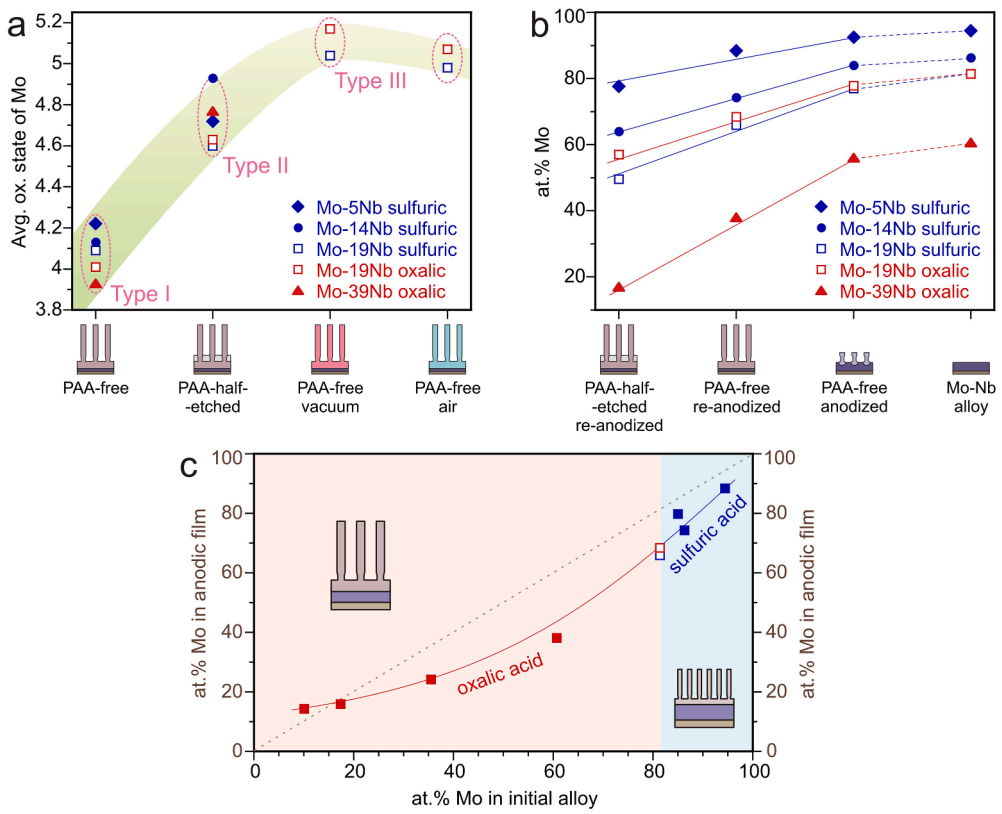


Fig. 6. Comparative analysis of the anodic films prepared in 0.6 M oxalic and 0.2 M sulfuric acid electrolytes. (a) An average oxidation state (AOS) of Mo cations in the anodic films derived from Mo-Nb alloys with various Mo contents, as depicted below the *x*-axis. (b) Mo content (Mo + Nb = 100 at. %) in the anodic films derived from various Mo-Nb alloys, as depicted below the *x*-axis. The last points show the Mo contents in the corresponding alloys. (c) Mo content in the anodic films vs. Mo content in the corresponding alloys.

19Nb alloy (Fig. 5c) contains, in addition to Al^{3+} and Al^{3+}–OH, about 12 % Al^0, which is due to a thin systematic network of non-anodized aluminum covering the alloy residues, as discussed in Section 3.2. The Al 2p spectrum of the re-anodized PAA-free film (Fig. 5f) has no Al° contribution, which implies that the aluminum residues were fully oxidized during the re-anodizing. The spectrum of the PAA-half-etched sample (Fig. 5i) also contains a minor amount of Al^{3+}–OH coordination. The amount of Al^{3+} at the surface of the OX nanorods ranges from 45 to 80 at. % (giving at. %(Al+Nb+Mo) = 100 %). The presence of alumina in the outer layer of metal-oxide nanorods seems typical for PAA-assisted anodizing of pure, mixed, or laminated metals reported to date (N-doped TiO_2 [38], Se-doped Nb_2O_5 [39], Se-doped ZrO_2 [26], or Mo-Nb oxide [16]), and it will receive detailed consideration in relation to the electronic properties of the nanoarrays developed in the present study.

3.3.4. *Heat-driven modifications*

The Mo 3d spectra of the *air- and vacuum-annealed* PAA-free films synthesized from Mo-19Nb alloy in the OX electrolyte appeared surprisingly comparable; the spectrum of the vacuum-annealed sample is shown in Fig. 5j. A few differences are noted when comparing with the as-prepared films. These are a substantially larger content of Mo^{6+} relative to the lower-valency cations, the presence of crystalline MoO_2 (~15 %), associated with the lowest binding energy doublet (see ESI for more details) [40,41], and an amount of Mo^{6+}–OH(H_2O) coordination in a hydrated MoO_3 oxide after the annealing. From Fig. S5, it is assumed that the bottom layer of the annealed films comprises a noticeable amount of crystalline MoO_2 (~60 %), while the rods grow in a fully amorphous manner, as follows from the spectrum of the annealed PAA-half-etched film (not shown). There is still a substantial contribution of Mo^{5+}, Mo^{4+}, and Mo^{3+} doublets to the recorded Mo 3d spectrum of the annealed films (Fig. 5j). The AOS value of Mo rises to 5.07 and 5.17 in the vacuum- and air-annealed films, respectively (Type III MoO_x), meaning a substantial oxidation of the oxides due to the annealing (Fig. 6a).

The Nb 3d spectra reveal that the surface layer of the PAA-free vacuum-annealed film (Fig. 5k), similarly to its as-prepared counterpart (Fig. 5e), contains a dominating amount of Nb_2O_5 mixed with a minor amount of NbO_2. However, the content of Nb^{4+} species in the vacuum-annealed film is tenfold lower (~1 %) than in the as-prepared film (10 %) and somewhat lower than in the air-annealed film (3 %). From this comparison, the niobium oxide at the film surface becomes more oxidized due to high-temperature annealing in air, and particularly in vacuum.

In the Al 2p spectra, the contribution of Al^{3+}–OH coordination increases substantially, up to 50 at. %, upon annealing (see Fig. 5l for the vacuum-annealed sample as the representative case).

3.3.5. *Quantitative analysis of Mo content*

Based on the above considerations, the surfaces of the anodic films made in the OX and SU electrolytes comprise MoO_x mixed with varying amounts of NbO_x. Quantitative analysis of the Mo 3d and Nb 3d narrow spectra recorded for the PAA-free and PAA-half-etched anodic films formed from the various alloys in both electrolytes is summarized in Fig. 6b. The common trend is that the Mo content at the film surface increases in the following sample order: re-anodized PAA-half-etched < re-anodized PAA-free < anodized PAA-free films. The highest amount of Mo (92 at. %, giving at. %(Mo+Nb) = 100 %) was measured at the surface of the SU anodized sample derived from the Mo-5Nb alloy. Notably, no change in the Mo content was found in the re-anodized PAA-free anodic films with annealing in air and vacuum.

Fig. 6c shows the correlation between the Mo content in the alloys

and the Mo content at the surface of various re-anodized PAA-free films prepared in the OX and SU electrolytes. From Fig. 6c, the surface contents of Mo in the anodic oxides are somewhat lower than in the corresponding alloys. The only exception is the film derived from the Mo-90Nb alloy, which reveals a higher Mo content (14 at. %) than the precursor alloy (10 at. %).

3.3.6. *A look inside the rods*

The experiment described below aimed to reveal the oxide composition solely within the rods, excluding the surface of the rods. Two re-anodized PAA-inbuilt anodic films, which were formed in the OX electrolyte under the same conditions from Mo-19Nb and Mo-39Nb alloys, were examined by XPS. The effectiveness of this approach in analyzing the inner composition of the PAA-inbuilt nanorods has been justified in our previous work. The narrow-scan Mo 3d–Nb 3d XP spectra of the two films are presented in Fig. 7. The insets explain the analysis performed.

The combined Mo 3d–Nb 3d spectrum of the Mo-19Nb-based anodic film (Fig. 7a) discloses the presence of both Mo and Nb in the amounts of 65 and 35 at. %, respectively, at the rod tops. In contrast, no Mo is found in the Mo-39Nb-based anodic film (Fig. 7b, see the ESI for further details). It is assumed that NbO_x-rich 'nanocaps' form on the rods derived from the Mo-39Nb alloy, originating from apparently faster migration of Nb cations relative to Mo cations in the mixed oxide during the re-anodizing of this alloy. However, the Nb content in the Mo-19Nb alloy is probably too low and, therefore, insufficient to enable a competitive migration of Nb cations and the formation of NbO_x-rich regions at the rod tops. The Mo-19Nb-based film (Fig. 7a) contains MoO_x reduced even more than Type I (AOS 3.54), which differs from the corresponding PAA-*half-etched* sample, having Type II MoO_x (AOS 4.63, see Fig. 5g). Moreover, the relatively high Mo content at the rod tops (65 at. %) suggests that the rods derived from the Mo-19Nb alloy rather have a uniform composition along their length. It is assumed that the reduced MoO_x resides inside the rod cores, while the more oxidized MoO_x is allocated on the surface. The Nb_2O_5 detected at the rod tops and likely residing inside the rods and at their surface is a defectless stoichiometric Nb_2O_5, which is mixed with MoO_x.

3.3.7. *Reaching the record high Mo content*

The SU electrolyte appeared to be the only solution for challenging anodizing of Mo-Nb alloys with a Mo content as high as 95 at. % (Fig. 8a and b). The Mo 3d, Nb 3d, Al 2p, and S 2p spectra of anodic films synthesized from the Mo-5Nb alloy in the SU electrolyte are shown in part in Fig. 8 and in full in Fig. S6. Generally, the recorded narrow-scan spectra of all films made in the SU electrolyte appeared similar to those made in the OX electrolyte. Typically, the analysis confirmed the presence of similar Types of MoO_x, NbO_x, as well as Al_2O_3, and Al–OH coordination in the corresponding parts of the SU film. The common trends in the evolution of chemical compositions and bonding states of the oxides formed in both electrolytes are seen in the plots of Fig. 6a and b, which summarize the XPS results collected for various Mo-Nb alloys. Most significantly, the Mo content detected at the surface of the re-anodized PAA-free SU film is 88 at. %, which is the highest achieved in this study after re-anodizing (Fig. 8c and Fig. S6, upper row).

In addition, the surface of the SU nanoarrays contains *sulfur*, in the amount of 0.5–1.5 at. % (giving at. %(S+Al+Mo+Nb) = 100 %), as shown in the representative S 2p spectrum in Fig. 8d. The presence of sulfur is also seen in the Mo 3d spectra as the S 2s peak of sulfate anions (234.0±0.2 eV), whose contribution is more considerable in the spectra of the PAA-half-etched films (Fig. S6e, the S 2s peak was subtracted for calculating Mo contents).

The vacuum- and air-annealing produced a similar impact on the SU and OX films in terms of Mo to Nb ratio, oxidation degree of Mo and Nb oxides, formation of crystalline MoO_2 (30 %), and high contribution of Al^{3+}–OH coordination, as follows from the analysis of XP spectra in Fig. S6, lower row. The difference, however, was in the amount of alumina at the rods' surface, which appeared unexpectedly low (35 at. %, giving at. %(Al+Mo+Nb) = 100 %) upon the annealing of the re-anodized SU anodic films.

Summarizing the XPS results and their interpretation: (a) The surface

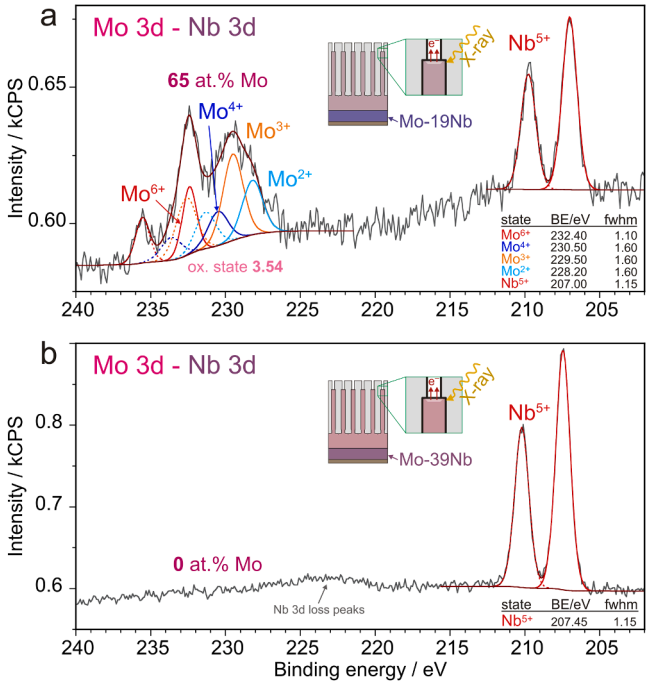


Fig. 7. Experimental and curve-fitted narrow-scan Mo 3d – Nb 3d XP spectra of PAA-inbuilt anodic films derived from (a) Mo-19at.%Nb alloy and (b) Mo-39at.%Nb alloy. Both films were synthesized via PAA-assisted anodizing in 0.6 M oxalic acid at 45 V, followed by re-anodizing to 300 V.

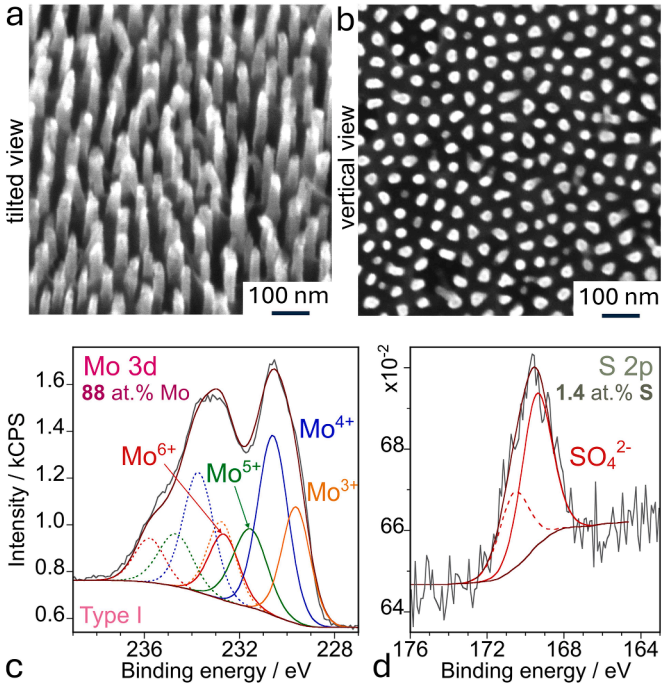


Fig. 8. (a, b) SEM images of an anodic film synthesized via anodizing/re-anodizing an Al/Mo-5at.%Nb bilayer in 0.2 M sulfuric acid at 25/105 V followed by selective PAA dissolution. (c, d) Experimental and curve-fitted narrow-scan Mo 3d and S 2p XP spectra of the film, confirming the highest achieved Mo content in the re-anodized film and the presence of sulfate.

layer of the oxide nanostructures is composed of molybdenum oxides with various Mo^{n+} cations ($n = 6$ to 3), Nb_2O_5 full oxide, NbO_2 suboxide, and Al_2O_3 mixed at the atomic level. (b) The oxides inside the rods and the bottom layer are alumina-free and more reduced than the oxides at the rods' surface. (c) A network of Al superimposed on the Mo-Nb alloy remains unoxidized in the anodized samples; it is gradually consumed during the re-anodizing. (d) The surface Mo content in the oxides systematically increases with Mo content in the corresponding alloys and can reach 92 at. % in the SU nanostructures. (e) The migration rate of Mo cations in the mixed oxides increases relatively to that of Nb cations with increasing Mo content in the alloy above ~61 at. %, allowing MoO_x to grow up to the rod tops. (f) The vacuum- and air-annealings make the substoichiometric molybdenum oxides substantially more oxidized and promote at least partial crystallization of molybdenum oxide in the bottom layer, which will be explored in detail in the following section.

3.4. Crystal structure of the alloy and oxide

The samples for XRD analysis were prepared by PAA-assisted anodizing of Mo-19Nb alloy in the OX electrolyte at 45 V, followed by re-anodizing to 300 V and annealing in air or vacuum at 550°C for 2 h. Fig. S7 shows the individual 2D and extracted conventional as-recorded, calculated, and difference diffractograms of the films. The crystal structures for all phases were identified using the ICDD and ICSD databases (FIZ, 2015). The main refinement parameters, details of the XRD line profiles, and the results of quantitative phase analysis are provided in the ESI. Fig. 9 compares the conventional diffractograms of each sample.

The *anodized* and *re-anodized* films (Fig. 9, two upper diffractograms) contain a polycrystalline Mo-Nb alloy phase, $Im\bar{3}m$ space group, crystallite size of 35 and 25 nm, respectively, <110> preferred orientation, which remains unoxidized below the anodic-oxide layers. The fitted cell dimension ($a = 3.181 \pm 0.001$ Å) falls between the values for pure Mo and Nb metals, yielding 21.0 ± 0.5 at. % Nb, which is in good agreement with the XPS-determined composition of the sputter-deposited Mo-19Nb alloy. The integrated intensity of the dominating (110) peak decreases in the re-anodized sample, apparently due to the thinning of the alloy layer

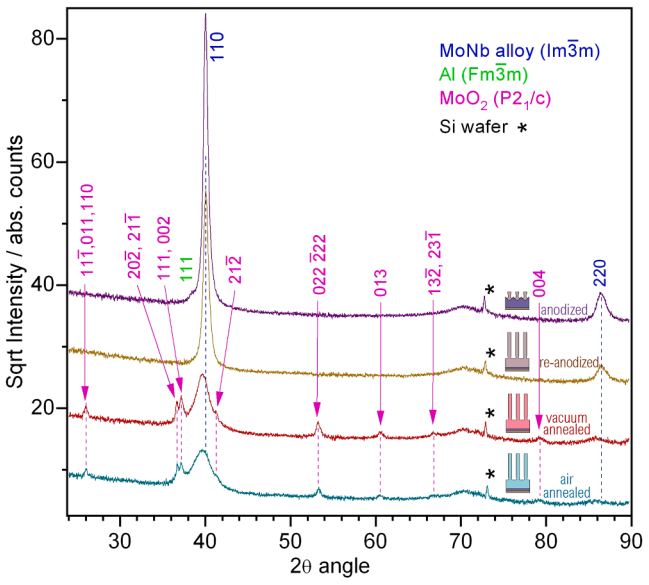


Fig. 9. Comparative X-ray diffractograms of anodic films synthesized from Mo-19at.%Nb alloy via PAA-assisted anodizing in 0.6 M oxalic acid at 45 V, followed by re-anodizing to 300 V, annealing the re-anodized film in vacuum (10^{-5} Pa) at 550°C for 2 h, or annealing the re-anodized film in ambient air at 550°C for 2 h. The PAA layers had been dissolved from each sample before the analysis was carried out.

during the re-anodizing process. The relatively larger crystallite size of the alloy in the anodized sample may be explained by the uneven distribution of crystallites across the alloy thickness: Smaller crystallites form closer to the substrate surface while the larger ones grow with the thickening of the alloy during the magnetron sputter-deposition, as noted elsewhere [42].

An amount of Al detected in the anodized sample (22 wt. %, crystallite size 15 nm) is associated with the aluminum residues surrounding the nanobulges. Since Al is not present in the re-anodized sample, the aluminum network was consumed during re-anodizing to 300 V, which is in agreement with the SEM and XPS results. Notably, totally amorphous oxides form during both anodizing and re-anodizing treatments under the selected electrical and electrolytic conditions.

The diffractograms of the *vacuum-* and *air-annealed re-anodized* films (Fig. 9, two lower patterns) reveal the presence of the same polycrystalline Mo-Nb alloy phase, which, however, is composed of significantly smaller nanocrystallites (~4 nm) with a substantially higher Nb content (41±1 at. %) relative to the non-annealed samples. These features are manifested by the broader (110) peak shifted to lower 2θ angles. Paradoxically, the integrated area of the (110) reflection is two-fold smaller in the annealed films than in the as-reanodized film, even though the SEM-determined thickness of the remaining alloy layer (~90 nm) seems unchanged after the annealing in both atmospheres. The seeming contradiction between the thickness of the remaining alloy and the shrunken area of the (110) reflection in the annealed samples will be explained in Section 3.5.2 with reference to the features of the film formation mechanism.

Furthermore, the monoclinic MoO_2 phase ($P2_1/c$ space group) in an amount of 50 wt. % is well identified in both vacuum-annealed and air-annealed films (crystallite size 29 and 18 nm, respectively); the refinement process is detailed in the ESI. No niobium-oxide phases are detected in the annealed films at the XRD resolution available. Since all the NbO_x phases in the ICSD database possess crystal structures dissimilar to monoclinic MoO_2, mixing the two crystalline oxides at the atomic level is highly unlikely, and only a minimal substitution of Mo^{n+} with Nb^{n+} might take place. Such mixing would be accompanied by a slight increase in cell parameters due to the different atomic radii of Nb (142 pm) and Mo (136 pm). As the average cell volume of monoclinic MoO_2 in the two annealed samples (131.0±0.1 $Å^3$) is even smaller than the average value reported in the ICDD database (131.8 $Å^3$), it is improbable that the monoclinic MoO_2 found in the annealed samples is mixed with NbO_x in an amount worth considering. Most likely, the MoO_2 nanocrystallites are separated from the niobium oxide and dispersed in an amorphous MoO_x-NbO_x matrix.

Generally, a similar trend in the alloy consumption and crystal-phase formation during re-anodizing and annealing was also revealed for the films synthesized from Mo-39Nb and Mo-5Nb alloys in the OX and SU electrolytes, respectively; minor differences are discussed in the ESI.

3.5. Film formation mechanism

3.5.1. Electrochemical aspects

It should be noted that, although several valve metals have been processed via PAA-assisted anodizing [35,43–47], there have been no reports on the success of this approach with molybdenum. Due to oxide instability [48,49], complemented by field crystallization [50], a slow migration rate of Mo cations [51], and an induction period in molybdenum anodizing [36], the PAA-controlled growth of solid oxides on Mo has been impossible. On the other hand, the relative migration rate of Mo^{n+} ions in a mixed oxide may change substantially, and even a minor addition of the second metal oxide might reportedly stabilize the growing anodic oxide [52,16]. Based on the SEM, XPS, and XRD results and their interpretation, we propose a model of oxide growth during the PAA-assisted anodic oxidation of Mo-Nb alloys with prevailing Mo content. The model will be represented by the Al/Mo-19Nb bilayer due to the challenging (critically low) content of Nb in this alloy, which still

allows PAA-assisted anodizing in the OX electrolyte and results in a high Mo content in the anodic oxide.

First, the upper Al layer (Fig. 10a) is transformed into a PAA layer. Once the PAA barrier layer touches the alloy, which is reflected by the beginning of current decay in Fig. 2c, the dot-like growth of Mo-Nb mixed oxide begins at the PAA barrier layer/alloy interface, as reported for anodizing Al/Nb [35] and Al/Ta [19] couples and suggested in the left inset of Fig. 2c. During the current decay, the growing anodic oxide on the Mo-Nb alloy penetrates the PAA barrier layer and pushes its way outward, filling the narrow channels that form in the PAA barrier layer due to its partial local dissolution under the field. The formation of nanobulges (Fig. 10b) occurs due to the same reasons as reported elsewhere [35]. A feature worth considering is the presence of protuberances from the tops of the bulges. They likely form during the current rise, which follows the current decay owing to enhanced dissolution of the anodic oxide that forms during the current rise. At the end of the anodizing stage, the aluminum residues are still present in the form of a continuous network surrounding the nanobulges. The formation of such a network is explained by the significant difference in ionic resistances between alumina and niobium (or molybdenum) oxides [26,35,53].

During re-anodizing, the remaining aluminum network is gradually consumed, while the alloy continues to oxidize, and the mixed-oxide nanorods grow outward within the pores (Fig. 10c). The Al consumption competes with further oxidation of the alloy, resulting in the expansion and merging of the bottom oxide area into a continuous bottom layer. With increasing re-anodizing voltage, the oxide/alloy interface loses its concave-like morphology and becomes relatively flat at ~220 V (Fig. 10d) and completely flat at 300 V (Fig. 10e). Two regions can be distinguished within the oxide nanorods: the inner one that forms solely inside the pores and the outer one that forms partly mixed with the PAA cell wall. The outer region forms due to the concurrent migration of Mo^{n+} (n = 3–6) and Nb^{5+} cations [19,35] in the PAA cell walls. The degree of mixing of the molybdenum and niobium oxides with Al_2O_3 in the PAA cell walls depends on the cell wall composition and its dissolution during the oxide growth [54]. As a result of the multi-cation migration in the 'pre-formed' alumina, the outer layer of the oxide nanorods comprises molybdenum oxides (Mo^{6+}, Mo^{5+}, Mo^{4+}, and Mo^{3+}), stoichiometric Nb_2O_5, and Al_2O_3 mixed at the atomic level (Fig. 10e).

In contrast with the rods' surface, the inner oxide is free from alumina; it is composed of a mixture of relatively more reduced molybdenum oxides (AOS ~3.5) and stoichiometric Nb_2O_5 because it forms exclusively via migration of the Mo and Nb cations in a pure Mo-Nb anodic oxide within the pores. The smooth formation of pure Mo-Nb mixed oxides within the pores is a unique phenomenon, as oxide growth on the Mo-19Nb alloy is not possible without a superimposed Al layer. The achievement is likely due to the oxide confinement within the nanosized PAA pores. Moreover, the narrower the pores become, the higher the Mo content can be afforded in the alloy that allows anodizing (Fig. 1).

The bottom oxide layer also contains significantly reduced molybdenum oxides (AOS of Mo ~3.5 at the surface) and niobium oxides (AOS of Nb ~4.8). It is estimated that the Mo content may be as high as 90 at. % inside the bottom layer (giving at. %(Mo+Nb) = 100 %), which forms entirely by the inward migration of O^{2-} anions. The oxide composing the rod outer layer is relatively more oxidized (AOS of Mo 4.6), but it contains less Mo, averaging around 60 at. %. This is likely because partial electrochemical dissolution of the oxide occurs during the re-anodizing and, under the high electric field, some Mo cations are expelled in the electrolyte without meeting oxygen anions at the electrolyte/oxide interface and, therefore, not contributing to anodic oxide growth, as typically occurs during anodic oxidation of aluminum [55] and other valve metals [56,57]. The PAA-assisted anodizing of molybdenum is more complex because of the specific molybdenum solution chemistry [58]. Since the anodizing electrolyte has an acidic pH, the expelled and dissolved Mo cations may participate in the formation of stable negatively charged polyoxometalates, such as the Lindqvist hexamolybdate, $Mo_6O_{19}^{2-}$ [59] or the Keggin's polyoxoanion, $P[Mo_{12}O_{40}]^{3-}$ [60,61]. Various negatively charged polyoxomolybdates might be adsorbed on the surface and get incorporated in the growing oxide under the high electric field, which makes the material of the rod cores less dense and more hydrated. With reference to our early work on PAA-assisted anodizing of tungsten [43], where some polyoxotungstates [62] were found inside the WO_x nanorods, it is assumed that the protuberances marked in Fig. 3a comprise polyoxomolybdates, and their

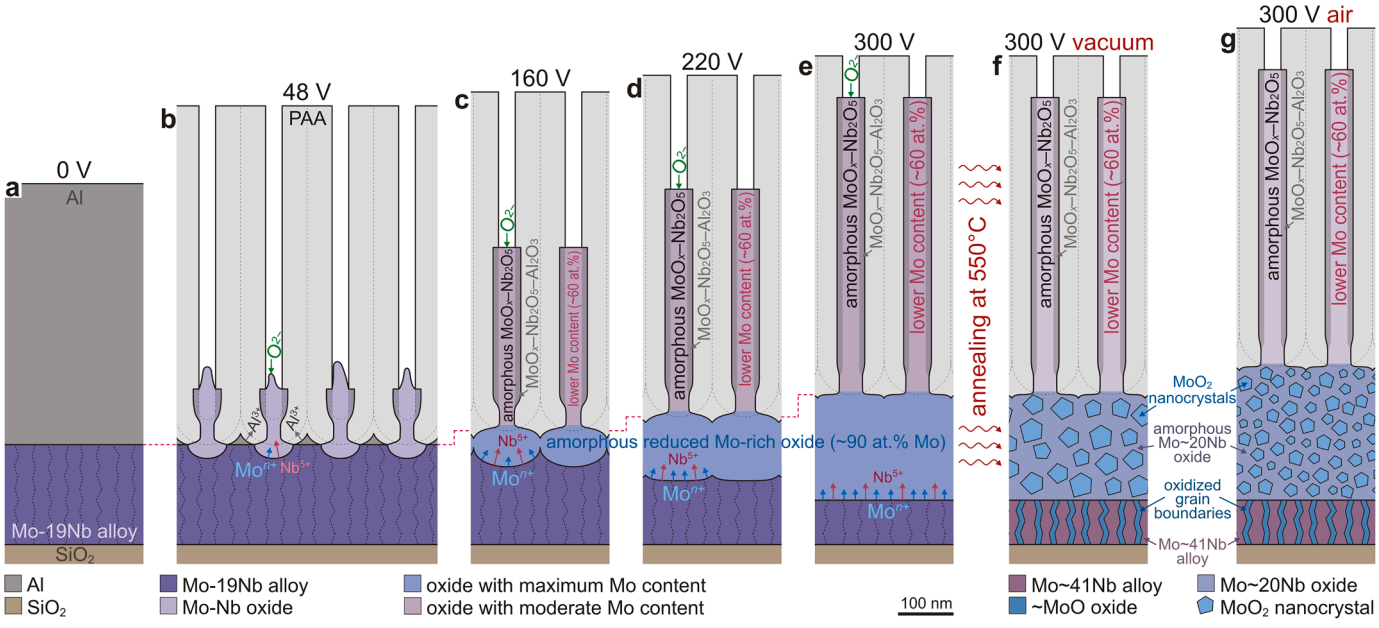


Fig. 10. The model of film growth: (a) the sputter-deposition of Al/Mo-19at.%Nb bilayer, as an example, (b) the anodizing of Al in 0.6 M oxalic acid at 45 V, finishing with the formation of nanobulges at the PAA/alloy interface, (c, d, and e) the re-anodizing to respectively 160, 220, and 300 V to grow oxide nanorods and the bottom-oxide layer of increasing thicknesses, (f) the annealing in vacuum (10^{-5} Pa, 550°C, 2h), and (g) the annealing in air (550°C, 2h).

shape is due to partial peripheral oxide dissolution inside each pore.

3.5.2. Paradoxical heat-treatment effect

All the anodic oxides composing the anodized and re-anodized films are entirely amorphous. The complex impact of the heat treatment on the alloys and anodic films deserves special consideration. Taking into account the quantitative XRD and XPS data analysis, complemented by the cross-sectional SEM observation, we propose the following mechanism. Although the annealing under the selected conditions (550°C for 2 h) does not impact the thickness of the remaining alloy, a small fraction of the alloy is, nevertheless, partially oxidized *along the alloy grain boundaries*. The preferential oxidation of Mo accompanies this process, while the Nb leaves the oxide and dissolves in the remaining alloy layer. This happens because the bond energy of O–Mo is higher than that of O–Nb (359 vs. 328 kJ/mol), resulting in a higher affinity of Mo for oxygen. Therefore, the intergranular thermal oxide is almost pure and likely amorphous MoO_x. The unoxidized fraction of the alloy becomes enriched with Nb, which induces its recrystallization at the applied temperature, resulting in a shrinking of the crystallite size to ~4 nm. The suggested structure of the alloy layer after annealing is depicted in Fig. 10f and g. A combination of factors, including phase separation and preferential thermal oxidation of Mo, reduction of alloy volume, and weakening of the preferred orientation in the alloy (see ESI), explains the paradoxically decreased integrated area of the (110) reflection of the Mo-Nb alloy phase after annealing.

The source of oxygen for the oxidation of grain boundaries is assumed to be O^{2-} anions from the bottom oxide, participating in the following reactions:

$$O^{2-} \rightarrow O^0 + 2e^- \text{ (oxidation of } O^{2-} \text{ anions in the bottom oxide)} \quad (1)$$

$$Mo^{n+} + e^- \rightarrow Mo^{(n-1)+} \text{ (reduction of } MoO_x \text{ in the bottom oxide by the generated electrons)} \quad (2)$$

$$Nb^{5+} + e^- \rightarrow Nb^{4+} \text{ (reduction of } Nb_2O_5 \text{ in the bottom oxide by the generated electrons)} \quad (3)$$

$$O^0_{oxide} \rightarrow O^0_{metal} \text{ (oxygen atom diffusion from the bottom oxide into the alloy grain boundaries)} \quad (4)$$

$$Mo + O^0 \rightarrow Mo^{II}O \text{ (preferred oxidation of Mo along the grain boundaries)} \quad (5)$$

Furthermore, the amorphous oxide in the bottom layer of the re-anodized sample (Fig. 10e) contains approximately 10 at. % Nb and undergoes a phase separation during the annealing: Nb^{n+} cations diffuse away from nanosized local areas, which become MoO_2 nanocrystals, and form an amorphous oxide matrix with about 20 at. % Nb, as shown in Fig. 10f and g. The driving force for this process is the favored formation of MoO_2 nanocrystals. The bottom oxide becomes thicker and more oxidized due to air annealing (AOS of Mo increases from ~3.5 to ~4.7; the amount of Nb^{4+} cations decreases from ~20 % to 2–5 %), indicating an uptake of oxygen from the ambient atmosphere. The nanorods remain amorphous after annealing, and their surface also becomes more oxidized compared to the as-reanodized samples (AOS of Mo increases from ~4.75 to ~5.55); they are still more oxidized than the bottom oxide is.

The paradoxical oxidation of the anodic films due to the annealing in vacuum can be explained as follows: Under the heat, the O^{2-} anions in the molybdenum oxides inside the rods and in the bottom layer are oxidized into O atoms and electrons, according to Eq. 1. The released electrons reduce the corresponding oxides (Eqs. 2 and 3), whereas the formed O atoms diffuse, due to the low residual pressure, from inside toward the film surface, where they further oxidize the sub-stoichiometric oxides:

$$Mo^{V}_2O_5 + O^0 \rightarrow 2Mo^{VI}O_3 \text{ (oxidation of Mo oxide by O atoms)} \quad (6)$$

$$2Nb^{IV}O_2 + O^0 \rightarrow Nb^{V}_2O_5 \text{ (oxidation of Nb oxide by O atoms)} \quad (7)$$

This vacuum-annealing-related mechanism appears to produce a more substantial surface oxidation effect than the classical oxygen uptake during heating in air. Therefore, the surface of the vacuum-annealed film becomes more oxidized than the surface of air-annealed films. Due to the above reasons, the inner oxides in the vacuum-annealed film become more reduced than those in the air-annealed film. The disclosed differences in annealing effects may significantly impact the electrical and electrochemical properties of the nanoarrays, which will be explored in Section 3.6.

3.6. Functional properties and application perspectives

3.6.1. Electrochemical energy storage

The anodic film synthesized via PAA-assisted anodizing of Mo-19Nb alloy in the OX electrolyte, followed by re-anodizing to 200 V and annealing in vacuum at 450°C for 3 h, was examined by CV and EIS before (*PAA-inbuilt*) and after (*PAA-free*) selectively dissolving the porous alumina (Fig. 11). The ***PAA-inbuilt*** sample (Fig. 11a, blue curve) reveals a noticeable anodic current in the first CV cycle (2 μA cm^{-2} at around −0.55 V *vs.* Ag/AgCl), which further increases to 4 μA cm^{-2} over the following ten CV scans (Fig. S8a). During the cathodic sweep, the current rises significantly below −0.7 V *vs.* Ag/AgCl, reaching −10 μA cm^{-2} at −1.0 V *vs.* Ag/AgCl. The cathodic current continues to rise, reaching a maximum of −14 μA cm^{-2}, with further CV cycles. Such a behavior seems relevant to the *n*-type semiconducting Mo-Nb-based anodic oxide residing in the dielectric PAA matrix: A depletion layer forms at the tops of the rods under more positive potentials and

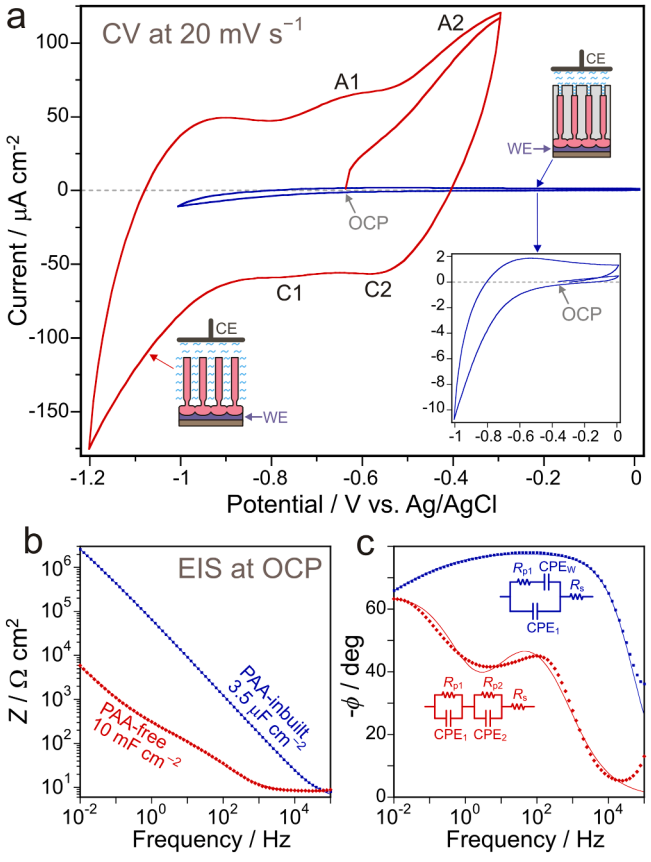


Fig. 11. Comparative electrochemical measurements performed with an anodic film first before (blue curves) and then after (red curves) the dissolution of the PAA layer. The film was prepared via PAA-assisted anodizing/re-anodizing of Mo-19at.%Nb alloy in 0.6 M oxalic acid (45/200 V), followed by annealing in vacuum (10^{-5} Pa) at 450°C for 3 h. (a) Cyclic voltammograms recorded at 20 mV s^{-1}. (b and c) Experimental (symbols) and fitted (lines) Bode plots obtained at OCP for each film: (b) modulus of impedance and (c) phase shift.

diminishes at negative potentials. The vanishing of the depletion layer allows for the incorporation of Na^+ or H^+ cations into the anodic oxide at potentials below −0.7 V *vs*. Ag/AgCl [16].

After dissolving the PAA overlayer, a 30-fold increase in the measured current is noted for the ***PAA-free*** film (Fig. 11a, red curve). Obviously, the dramatically increased current in the PAA-free film is associated with a 28-fold increase in the effective surface area. Moreover, the CV curves change their behavior after the PAA dissolution, showing clear signs of pseudocapacitive properties of the anodic film, such as a rectangular CV shape, several broad cathodic and anodic peaks (C1, C2, A1, and A2, marked in Fig. 11a), and the fulfillment of the 'mirror image' criterion [63] (see for the additional CVs in Fig. S8). The peaks are associated with the reversible insertion/extraction of Na^+ cations [4,64], while the rise of the cathodic current below −1.0 V vs. Ag/AgCl may be caused by the irreversible hydrogen evolution reaction [16].

The semiconducting nature of the nanorods is eventually confirmed by the EIS measurements at OCP (−0.37 and −0.64 V *vs*. Ag/AgCl for the PAA-inbuilt and PAA-free films, respectively). The Bode plot obtained for the PAA-inbuilt sample (blue curves in Fig. 11b and c) is fitted with an equivalent electrical circuit containing a CPE and a Warburg impedance (inset in Fig. 11c), resulting in a capacitance of 3.5 μF cm^{-2} (18 μF cm^{-2} relative to the effective area, A_e, which is ~20 % of the apparent surface area). Assuming a relative permittivity $\varepsilon_r = 35$, the calculated thickness of the depletion layer $d = 1.8$ nm, which is way smaller than the thickness of the anodic film (~480 nm). The resistivity of the depletion layer is calculated as $\rho = R_{p,e}/d$, where $R_{p,e}$ is the parallel resistance of the depletion layer related to A_e, resulting in $\rho = 0.1$ MΩ cm^2 nm^{-1}. The presence of Warburg impedance is attributed to the diffusion of ions within the PAA nanopores [65]. The Mott-Schottky measurements (not shown) confirmed that the anodic oxide inside the PAA nanopores is indeed an *n*-type semiconductor with a high donor concentration, $N_d = \sim 2 \times 10^{21}$ cm^{-3}.

The Bode plot of the PAA-free film (red curves in Fig. 11b and c) shows a 300-fold decrease in impedance value, which is even higher than one might expect from the increase in the effective surface area. Furthermore, the two time constants enable fitting the measured curves with an equivalent electrical circuit comprising two CPEs, as shown in the inset of Fig. 11c. The first CPE-R_p couple with the higher R_p value represents the depletion layer that forms over the entire surface of the anodic film, combined with the pseudocapacitance of the film. The extraordinarily high measured capacitance of about 10 mF cm^{-2}, which corresponds to ~1.8 mF cm^{-2} when recalculated for $A_e = 570$ %, is 100 times bigger than that calculated for the PAA-inbuilt anodic film. The second CPE-R_p couple, with the lower R_p value, is assigned to the Helmholtz layer formed at the electrolyte/oxide interface. The complete set of fitted parameters for the PAA-inbuilt and PAA-free samples is available in the ESI (Table S5).

From the electrochemical analysis, the entire surface of the PAA-free film is a highly doped *n*-type semiconductor. Moreover, except for the tops of the rods (~4 % of the entire surface), the outer layers of the protruding parts and the bottom oxide (550 % of the apparent surface area), exhibiting distinctive pseudocapacitive properties, are available for effective electron transport and surface reactions. The achievement is attributed to the high content of MoO_x at the surface of the mixed-oxide nanorods, which approaches ~90 at. % in the bottom-oxide layer.

Comparing the present result with our previous report on the PAA-assisted anodizing of an Nb/Mo laminate [16], a noticeable difference is observed: In the previous case, only the rod cores, not the film surface, exhibited pseudocapacitive properties, which severely limited the energy-related application potential [16]. In the present case, the entire surface of the nanoarrays reveals the pseudocapacitive properties. The 30-fold increase in effective surface area results in a 3×10^3 increase in capacitance and a 30-fold higher current collected over the PAA-free film surface. Both features, complemented by the compatibility of the formation methods with standard micro- and nanofabrication technologies, render the films perfect candidates for on-chip energy-storage applications. An in-depth investigation of the pseudocapacitive properties of the nanoarrays developed in this study, including deconvolution of the measured current into the capacitive and diffusive contributions and justification of reversible and irreversible electrochemical processes at the electrode, will be the subject of a detailed follow-up investigation.

3.6.2. *Gas-sensing performance*

The high surface-to-volume ratio of the nanostructured MoO_x-based anodic oxides, with a large number of reactive sites on their surfaces, seemed promising for testing the films as the active layers for chemiresistive gas sensors. An Mo-9Nb alloy layer was selected for this experiment as one of the options with a high Mo content (see Fig. 1). Anodizing was carried out in the SU electrolyte (25/105V), followed by annealing in ambient air at 550°C for 5 h. A longer annealing time was required to fully oxidize the alloy remaining after re-anodizing below the bottom oxide layer. Gas-sensing experiments were conducted in *ethanol* and *carbon monoxide* diluted with synthetic air by measuring the in-plane resistance between two parallel conducting strips on the film surface in the presence of each gas (Fig. 12a).

It should be noted that the resistance decreased reversibly with increasing temperature from 25 to 300°C when measured in air without any gas (data not shown), a typical behavior for an *n*-type semiconductor. As an example, Fig. 12b illustrates a series of normalized sensor responses to pulses of ethanol followed by CO pulses at 250 and 300°C. The quantitative analysis reveals that the sensor response to 10 ppm ethanol is fast, with a response time of ~80 s at each temperature, while the recovery time is relatively longer and improves with increasing temperature. The sensor rapidly reacts to and recovers from low-concentration CO, especially at 300°C. In terms of sensitivity and response time to each gas, the present film surpasses the previously reported Zr-W mixed-oxide nanofilm [66]. The inverted sensor response to CO can be a factor that helps discriminate between the two gases, which is beneficial for practical applications. We assume that such an unusual response to CO, which is a typical reducing gas [67], occurs due to

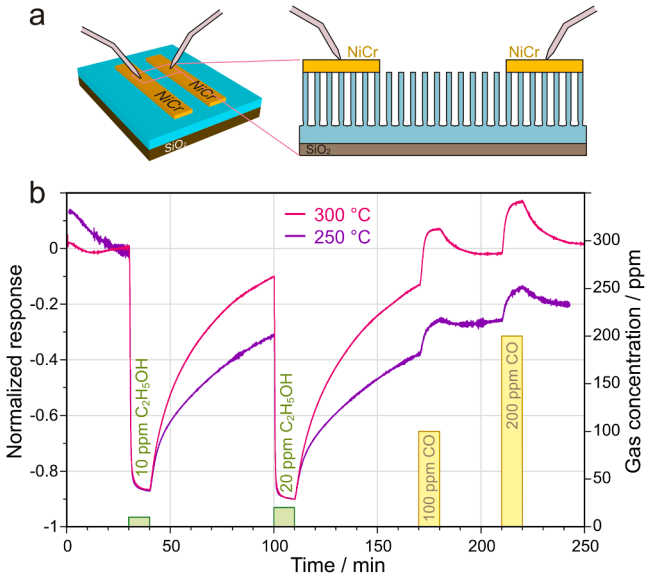


Fig. 12. (a) Schematics of a 3D view and cross-sectional fragment of a microchip utilizing a nanostructured anodic film as the active layer for gas-sensing tests. The film was synthesized from Mo-9at.%Nb alloy via PAA-assisted anodizing/re-anodizing at 25/105 V in 0.2 M sulfuric acid, followed by annealing in air at 550°C for 5 h. (b) Normalized responses of the sensor chip to pulses of C_2H_5OH and CO at 250 and 300°C. The response is defined as $(R_{gas}-R_0)/R_0$, where R_0 is the baseline resistance in air, and R_{gas} is the resistance in the presence of a test gas.

concurrent chemical reactions specific to this nanofilm, which is highly enriched with molybdenum oxides-hydroxides. The major revelation from the present tests is that the semiconducting nanoarrays derived from the Mo-Nb alloy with a prevailing molybdenum content (88 at. % Mo) can be an on-chip sensor solution for highly sensitive and possibly selective detection of low concentrations of harmful/toxic gases. A comprehensive study of the gas-sensing properties of the Mo-Nb mixed oxides with variable Mo contents and morphologies is currently underway, yielding exciting results that will be reported in a specialized paper.

4. Conclusions

The following major conclusions may be drawn from the present study.

1. MoO_x-rich nanostructures, such as bulges, columns, and rods, were synthesized in the form of self-standing protrusions on a substrate via a highly challenging in situ PAA-assisted anodizing of sputter-deposited Mo-Nb alloys with a variable Mo content reaching 95 at. %. There have been no reports competing with the present achievement.
2. The surfaces of the nanostructures typically comprise a dominant amount of MoO_x with various Mo^{n+} cations ($n = 6$ to 3) mixed at the atomic level with minor amounts of Nb_2O_5 full oxide, NbO_2 sub-oxide, and Al_2O_3. The latter originates from the PAA pore walls and 'serves' as a shape stabilizer.
3. Upon annealing at 550°C, the entirely amorphous as-prepared anodic oxides undergo a rare phase separation followed by the formation of MoO_2 nanocrystals dispersed in the amorphous MoO_x-Nb_2O_5 solid solution within the bottom-oxide layer.
4. Both the outer and inner oxides in the nanoarrays are highly doped *n*-type semiconductors, with a donor concentration of $\sim 2 \times 10^{21}$ cm^{-3} upon annealing.
5. From the application perspective, the entire surface of the nanostructured film grown from the Mo-19Nb alloy exhibited distinctive pseudocapacitive properties, with a capacitance of ~10 mF cm^{-2}, rendering the film auspicious for integration in on-chip supercapacitors. Moreover, the film proved highly efficient as the active layer of a gas microsensor, capable of rapidly detecting low concentrations of C_2H_5OH (response time ~80 s) and CO, due to the structuring and high surface content of hydrated MoO_3 oxide. More potential applications are envisioned, such as in biomedicine (antibacterial films) or protective coatings (self-cleaning and water- and oil-repellent surfaces), as well as electro- and photochromic layers, where high-density, rod-like nanomorphologies rich in Mo-containing reactive sites are highly sought after [1,13,14].
6. All in all, this work confirms that the challenge of synthesizing fully semiconducting arrays of MoO_x-based multifunctional nanostructures with a dominant amount of Mo, reaching 92 at. %, and up to almost 8 times enlarged effective surface area, has been met. The present accomplishments substantially advance the state-of-the-art MoO_x-based nanomaterials and their fabrication nanotechnologies, including those reported in our preceding work [16].

CRediT authorship contribution statement

Alexander Mozalev: Writing – review & editing, Writing – original draft, Visualization, Supervision, Resources, Project administration, Methodology, Investigation, Funding acquisition, Conceptualization. **Maria Bendova:** Writing – original draft, Visualization, Validation, Methodology, Investigation, Formal analysis. **Jan Prasek:** Investigation. **Lukas Kalina:** Investigation, Data curation. **Petr Smisitel:** Visualization, Investigation. **Francesc Gispert-Guirado:** Visualization, Validation, Investigation. **Eduard Llobet:** Writing – review & editing, Resources, Funding acquisition.

Declaration of competing interest

The authors declare that they have no known competing financial interests or personal relationships that could have appeared to influence the work reported in this paper.

Acknowledgments

This research was financially supported by the Czech Science Foundation (GACR), project no. 23-07848S. The CzechNanoLab project LM2023051, funded by the MEYS CR, is acknowledged for the sputter deposition of metal layers. E.L. was supported by the Catalan Institution for Research and Advanced Studies via the 2023 Edition of the ICREA Academia Award and by the Spanish Agency for Research (AEI) and FEDER via grant no. PID2022-142451OB-C21.

Supplementary materials

Supplementary material associated with this article can be found, in the online version, at doi:10.1016/j.apsadv.2026.100950.

Data availability

Data will be made available on request.

References

[1] T.R. Lenka, H.P.T. Nguyen, Nanoelectronic Devices and Applications, Bentham Science Publishers, 2024, https://doi.org/10.2174/9789815238242124010 1.
[2] R. Malik, N. Joshi, V.K. Tomer, Advances in the designs and mechanisms of MoO_3 nanostructures for gas sensors: a holistic review, Mater. Adv. 2 (2021) 4190–4227, https://doi.org/10.1039/D1MA00374G.
[3] Y. Jiang, Y. Wang, J. Ni, L. Li, Molybdenum-based materials for sodium-ion batteries, InfoMat 3 (2021) 339–352, https://doi.org/10.1002/inf2.12175.
[4] A.E. Elkholy, T.T. Duignan, X. Sun, X. Song Zhao, Stable α-MoO_3 electrode with a widened electrochemical potential window for aqueous electrochemical capacitors, ACS Appl. Energy Mater. 4 (2021) 3210–3220, https://doi.org/10.1021/acsaem.0c02990.
[5] H. Wang, T. Li, A.M. Hashem, A.E. Abdel-Ghany, R.S. El-Tawil, H.M. Abuzeid, A. Coughlin, K. Chang, S. Zhang, H. El-Mounayri, A. Tovar, L. Zhu, C.M. Julien, Nanostructured molybdenum-oxide anodes for lithium-ion batteries: an outstanding increase in capacity, Nanomaterials 12 (2021) 13, https://doi.org/10.3390/nano12010013.
[6] B. Hu, L. Mai, W. Chen, F. Yang, From MoO_3 nanobelts to MoO_2 nanorods: structure transformation and electrical transport, ACS Nano 3 (2009) 478–482, https://doi.org/10.1021/nn800844h.
[7] Y. Jia, Y. Ma, Advances in MoO_3-based supercapacitors for electrochemical energy storage, J. Energy Storage 85 (2024) 111103, https://doi.org/10.1016/j.est.2024.111103.
[8] P.U. Nzereogu, A.D. Omah, F.I. Ezema, E.I. Iwuoha, A.C. Nwanya, Anode materials for lithium-ion batteries: A review, Appl. Surf. Sci. Adv. 9 (2022) 100233, https://doi.org/10.1016/j.apsadv.2022.100233.
[9] I.A. de Castro, R.S. Datta, J.Z. Ou, A. Castellanos-Gomez, S. Sriram, T. Daeneke, K. Kalantar-zadeh, Molybdenum oxides – From fundamentals to functionality, Adv. Mater. 29 (2017) 1701619, https://doi.org/10.1002/adma.201701619.
[10] K. Hermann, M. Witko, Chapter 4 – Theory of physical and chemical behavior of transition metal oxides: vanadium and molybdenum oxides, in: D.P. Woodruff (Ed.), Oxide Surfaces, Elsevier Science B.V., 2001, pp. 136–198, https://doi.org/10.1016/S1571-0785(01)80024-9.
[11] J. Bhattacharjee, S. Roy, Exploration of Molybdenum Oxide Compounds-A Review, Cataly. Res. 4 (3) (2024) 011, https://doi.org/10.21926/cr.2403011.
[12] A.A. Shaikh, J. Bhattacharjee, P. Datta, S. Roy, A comprehensive review of the oxidation states of molybdenum oxides and their diverse applications, Sustain. Chem. Environ. 7 (2024) 100125, https://doi.org/10.1016/j.scenv.2024.100125.
[13] M.G. Yirak, R. Chaujar, Fundamental of Emerging Nanomaterials, in: Y.S. Song, L. R. Thoutam, S. Tayal, S.B. Rahi, T.S.A. Samuel (Eds.), Handbook of Emerging Materials for Semiconductor Industry, Springer, Singapore, 2024, pp. 3–24, https://doi.org/10.1007/978-981-99-6649-3_1.
[14] P. Bhol, M.B. Bhavya, S. Swain, M. Saxena, A.K. Samal, Miniaturization on chip nano energy application, in: S.K. Shukla, C.M. Hussain, B. Mangla, M. Choudhary, S. Patra (Eds.), Nanotechnology in Miniaturization, An Emerging Trend to Fabricate Future Devices, Springer, 2024, pp. 173–196.
[15] G.A. Tsirlina, Electrochemical surface finishing in miniature—micro and nano electrochemical fabrication for physics and engineering, J. Solid State Electrochem. 29 (2025) 1265–1307, https://doi.org/10.1007/s10008-025-06245-w.
[16] A. Mozalev, M. Bendova, L. Kalina, J. Prasek, Francesc Gispert-Guirado, E. Llobet, MoO_x-based high-density nanoarrays on a substrate *via* smart anodizing as novel

3D electrodes for nano-energy applications, J. Mater. Chem. A 13 (2025) 19605–19622, https://doi.org/10.1039/D5TA02921J.
[17] J.T. Domagalski, E. Xifre-Perez, L.F. Marsal, Recent Advances in Nanoporous Anodic Alumina: Principles, Engineering, and Applications, Nanomaterials 11 (2) (2021) 430, https://doi.org/10.3390/nano11020430.
[18] C. Fernández-González, S. Ruiz-Gómez, A. Arché-Núñez, L. Pérez, C. Tavares de Sousa, Nano-patterning using ultra-thin alumina membranes, Mater. Today Nano 29 (2025) 100553, https://doi.org/10.1016/j.mtnano.2024.100553.
[19] A. Mozalev, M. Sakairi, I. Saeki, H. Takahashi, Nucleation and growth of the nanostructured anodic oxides on tantalum and niobium under the porous alumina film, Electrochim. Acta. 48 (2003) 3155–3170, https://doi.org/10.1016/S0013-4686(03)00345-1.
[20] A. Mozalev, R. Calavia, R.M. Vázquez, I. Gràcia, C. Cané, X. Correig, X. Vilanova, F. Gispert-Guirado, J. Hubálek, E. Llobet, MEMS-microhotplate-based hydrogen gas sensor utilizing the nanostructured porous-anodic-alumina-supported WO_3 active layer, Int. J. Hydrogen Energy 38 (2013) 8011–8021, https://doi.org/10.1016/j.ijhydene.2013.04.063.
[21] S. Ono, M. Saito, H. Asoh, Self-ordering of anodic porous alumina formed in organic acid electrolytes, Electrochim. Acta 51 (2005) 827–833, https://doi.org/10.1016/j.electacta.2005.05.058.
[22] C.S. Blackman, X. Correig, V. Katko, A. Mozalev, I.P. Parkin, R. Alcubilla, T. Trifonov, Templated growth of tungsten oxide micro/nanostructures using aerosol assisted chemical vapour deposition, Mater. Lett. 62 (2008) 4582–4584, https://doi.org/10.1016/j.matlet.2008.08.027.
[23] T. Kikuchi, A. Takenaga, S. Natsui, R.O. Suzuki, Advanced hard anodic alumina coatings via etidronic acid anodizing, Surf. Coat. Technol. 326 (2017) 72–78, https://doi.org/10.1016/j.surfcoat.2017.07.043.
[24] A. Mozalev, I. Mozaleva, M. Sakairi, H. Takahashi, Anodic film growth on Al layers and Ta–Al metal bilayers in citric acid electrolyte, Electrochi. Acta 50 (2005) 5065–5075, https://doi.org/10.1016/j.electacta.2005.02.092.
[25] V. Surganov, P. Morgen, J.G. Nielsen, G. Gorokh, A. Mozalev, Study of the initial stage of aluminium anodization in malonic acid solution, Electrochim. Acta 32 (1987) 1125–1127, https://doi.org/10.1016/0013-4686(87)90043-0.
[26] K. Kamnev, M. Bendova, Z. Fohlerova, T. Fialova, O. Martyniuk, J. Prasek, K. Cihalova, A. Mozalev, Arrays of ultra-thin selenium-doped zirconium-anodic-oxide nanorods as potential antibacterial coatings, Mater. Chem. Front. 9 (2025) 866–883, https://doi.org/10.1039/D4QM01081G.
[27] A. Mozalev, M. Bendova, F. Gispert-Guirado, E. Llobet, H. Habazaki, Porous-anodic-alumina-templated Ta-Nb-alloy/oxide coatings via the magnetron-sputtering/anodizing as novel 3D nanostructured electrodes for energy-storage applications, Surf. Coat. Technol. 489 (2024) 131042, https://doi.org/10.1016/j.surfcoat.2024.131042.
[28] B.P. Payne, M.C. Biesinger, N.S. McIntyre, X-ray photoelectron spectroscopy studies of reactions on chromium metal and chromium oxide surfaces, J. Electron. Spectrosc. Relat. Phenom. 184 (2011) 29–37, https://doi.org/10.1016/j.elspec.2010.12.001.
[29] H.M. Rietveld, A profile refinement method for nuclear and magnetic structures, J. Appl. Crystallogr. 2 (1969) 65–71, https://doi.org/10.1107/S0021889869006558.
[30] A.A. Coelho, TOPAS and TOPAS-Academic: An optimization program integrating computer algebra and crystallographic objects written in C++, J. Appl. Crystallogr. 51 (2018) 210–218, https://doi.org/10.1107/S1600576718000183.
[31] B. Hirschorn, M.E. Orazem, B. Tribollet, V. Vivier, I. Frateur, M. Musiani, Determination of effective capacitance and film thickness from constant-phase element parameters, Electrochim. Acta 55 (2010) 6218–6227, https://doi.org/10.1016/j.electacta.2009.10.065.
[32] A. Jagminas, I. Vrublevsky, Chapter three - Anodizing of aluminum under the burning conditions, in: G.D. Sulka (Ed.), Nanostructured Anodic Metal Oxides, Elsevier, 2020, pp. 89–122, https://doi.org/10.1016/B978-0-12-816706-9.00003-0.
[33] A. Mozalev, S. Magaino, H. Imai, The formation of nanoporous membranes from anodically oxidized aluminium and their application to Li rechargeable batteries, Electrochim. Acta 46 (2001) 2825–2834, https://doi.org/10.1016/S0013-4686(01)00497-2.
[34] K.S. Napolskii, I.V. Roslyakov, A.A. Eliseev, D.V. Byelov, A.V. Petukhov, N. A. Grigoryeva, W.G. Bouwman, A.V. Lukashin, A.P. Chumakov, S.V. Grigoriev, The kinetics and mechanism of long-range pore ordering in anodic films on aluminum, J. Phys. Chem. C 115 (2011) 23726–23731, https://doi.org/10.1021/jp207753v.
[35] A. Mozalev, R.M. Vázquez, C. Bittencourt, D. Cossement, F. Gispert-Guirado, E. Llobet, H. Habazaki, Formation–structure–properties of niobium-oxide nanocolumn arrays via self-organized anodization of sputter-deposited aluminum-on-niobium layers, J. Mater. Chem. C 2 (2014) 4847–4860, https://doi.org/10.1039/C4TC00349G.
[36] V.S. Saji, C.-W. Lee, Molybdenum, molybdenum oxides, and their electrochemistry, ChemSusChem 5 (2012) 1146–1161, https://doi.org/10.1002/cssc.201100660.
[37] D.N. Gopala Krishna, J. Philip, Review on surface-characterization applications of X-ray photoelectron spectroscopy (XPS): Recent developments and challenges, Appl. Surf. Sci. Adv. 12 (2022) 100332, https://doi.org/10.1016/j.apsadv.2022.100332.
[38] M. Bendova, J. Kolar, M. Marik, T. Lednicky, A. Mozalev, Influence of nitrogen species on the porous-alumina-assisted growth of TiO_2 nanocolumn arrays, Electrochim. Acta 281 (2018) 796–809, https://doi.org/10.1016/j.electacta.2018.05.197.
[39] K. Kamnev, M. Bendova, Z. Pytlicek, J. Prasek, L. Kejik, F. Guell, E. Llobet, A. Mozalev, Se-doped Nb_2O_5–Al_2O_3 composite-ceramic nanoarrays via the anodizing of Al/Nb bilayer in selenic acid, Ceram. Int. 49 (2023) 34712–34725, https://doi.org/10.1016/j.ceramint.2023.08.134.
[40] P.A. Spevack, N.S. McIntyre, Thermal reduction of MoO_3, J. Phys. Chem. 96 (1992) 9029–9035, https://doi.org/10.1021/j100201a062.
[41] D.O. Scanlon, G.W. Watson, D.J. Payne, G.R. Atkinson, R.G. Egdell, D.S.L. Law, Theoretical and experimental study of the electronic structures of MoO_3 and MoO_2, J. Phys. Chem. C 114 (2010) 4636–4645, https://doi.org/10.1021/jp9093172.
[42] R. Ramos, M. Chaves, E. Martins, S.F. Durrant, E.C. Rangel, T.F. da Silva, J.R. R. Boroleto, Growth evolution of AZO thin films deposited by magnetron sputtering at room temperature, Mat. Res. 24 (2021) e20210052, https://doi.org/10.1590/1980-5373-MR-2021-0052.
[43] A. Mozalev, M. Bendova, F. Gispert-Guirado, Z. Pytlicek, E. Llobet, Metal-substrate-supported tungsten-oxide nanoarrays via porous-alumina-assisted anodization: from nanocolumns to nanocapsules and nanotubes, J. Mater. Chem. A 4 (2016) 8219–8232, https://doi.org/10.1039/C6TA02027E.
[44] S.H. Park, Y.H. Kim, T.G. Lee, H.K. Shon, H.M. Park, J.Y. Song, Synthesis and electrochemical capacitance of long tungsten oxide nanorod arrays grown vertically on substrate, Mater. Res. Bull. 47 (2012) 3612–3618, https://doi.org/10.1016/j.materresbull.2012.06.053.
[45] A. Mozalev, M. Bendova, F. Gispert-Guirado, E. Llobet, Hafnium-oxide 3-D nanofilms via the anodizing of Al/Hf metal layers, Chem. Mater. 30 (2018) 2694–2708, https://doi.org/10.1021/acs.chemmater.8b00188.
[46] S.Z. Chu, K. Wada, S. Inoue, H. Segawa, Direct growth of highly ordered crystalline zirconia nanowire arrays with high aspect ratios on glass by a tailored anodization, J. Electrochem. Soc. 157 (2011) C148–C157, https://doi.org/10.1149/1.3568997.
[47] A. Mozalev, Z. Pytlicek, K. Kamnev, J. Prasek, F. Gispert-Guirado, E. Llobet, Zirconium oxide nanoarrays via the self-organized anodizing of Al/Zr bilayers on substrates, Mater. Chem. Front. 5 (2021) 1917–1931, https://doi.org/10.1039/D0QM00862A.
[48] B. Jin, X. Zhou, L. Huang, M. Lickleder, M. Yang, P. Schmuki, Aligned MoO_x/MoS_2 core–shell nanotubular structures with a high density of reactive sites based on self-ordered anodic molybdenum oxide nanotubes, Angew. Chem. Int. Ed. 55 (2016) 12252–12256, https://doi.org/10.1002/anie.201605551.
[49] M.R. Arora, R. Kelly, The structure and stoichiometry of anodic films on V, Nb, Ta, Mo and W, J. Mater. Sci. 12 (1977) 1673–1684, https://doi.org/10.1007/BF00542819.
[50] Ø.S. Fjellvåg, A. Ruud, H.H. Sønsteby, O. Nilsen, H. Fjellvåg, Crystallization, phase stability, and electrochemical performance of β-MoO_3 thin films, Cryst. Growth Des. 20 (2020) 3861–3866, https://doi.org/10.1021/acs.cgd.0c00156.
[51] H. Habazaki, M. Uozumi, H. Konno, K. Shimizu, S. Nagata, K. Asami, P. Skeldon, G. E. Thompson, Influence of molybdenum species on growth of anodic titania, Electrochim. Acta 47 (2002) 3837–3845, https://doi.org/10.1016/S0013-4686(02)00319-5.
[52] H. Habazaki, M. Uozumi, H. Konno, S. Nagata, K. Shimizu, Formation of barrier-type amorphous anodic films on Ti–Mo alloys, Surf. Coat. Technol. 169–170 (2003) 151–154, https://doi.org/10.1016/S0257-8972(03)00216-0.
[53] J.P.S. Pringle, The anodic oxidation of superimposed metallic layers: theory, Electrochim. Acta 25 (1980) 1423–1437, https://doi.org/10.1016/0013-4686(80)87157-X.
[54] I. Vrublevsky, V. Parkoun, V. Sokol, J. Schreckenbach, Study of chemical dissolution of the barrier oxide layer of porous alumina films formed in oxalic acid using a re-anodizing technique, Appl. Surf. Sci. 236 (2004) 270–277, https://doi.org/10.1016/j.apsusc.2004.04.030.
[55] G.E. Thompson, G.C. Wood, 5 - Anodic Films on Aluminium, Treatise on Mater. Sci. Technol. 23 (1983) 205–329, https://doi.org/10.1016/B978-0-12-633670-2.50010-3.
[56] J.P. Kollender, A.I. Mardare, A.W. Hassel, In-situ monitoring of metal dissolution during anodization of tantalum, J. Electrochem. Soc. 164 (2017) C598–C601, https://doi.org/10.1149/2.1471709jes.
[57] J.P. Kollender, C.C. Mardare, A.I. Mardare, A.W. Hassel, Downstream analytics quantification of ion release during high-voltage anodisation of niobium, J. Solid State Electrochem. 22 (2018) 2457–2464, https://doi.org/10.1007/s10008-018-3957-4.
[58] G. Tsirlina, Solutions of polyoxometalates: Ionic association and oversaturation as the factors affecting electrode surface modification, Meet. Abstr. MA2014-01 (2014) 1047. https://iopscience.iop.org/article/10.1149/MA2014-01/24/1047.
[59] M. Han, J. Hey, W. Kawamura, D. Stalke, M. Shionoya, G.H. Clever, An inclusion complex of hexamolybdate inside a supramolecular cage and its structural conversion, Inorg. Chem. 51 (2012) 9574–9576, https://doi.org/10.1021/ic301359n.
[60] M. Genovese, K. Lian, Polyoxometalate modified inorganic–organic nanocomposite materials for energy storage applications: A review, Curr. Opin. Solid State Mater. Sci. 19 (2015) 126–137, https://doi.org/10.1016/j.cossms.2014.12.002.
[61] J.-J.J. Chen, M.A. Barteau, Molybdenum polyoxometalates as active species for energy storage in non-aqueous media, J. Energy Storage 13 (2017) 255–261, https://doi.org/10.1016/j.est.2017.07.017.
[62] N.I. Gumerova, A. Rompel, Polyoxometalates in solution: speciation under spotlight, Chem. Soc. Rev. 49 (2020) 7568–7601, https://doi.org/10.1039/D0CS00392A.
[63] S. Fleischmann, J.B. Mitchell, R. Wang, C. Zhang, D. Jiang, V. Presser, V. Augustyn, Pseudocapacitance: From fundamental understanding to high power energy storage materials, Chem. Rev. 120 (2020) 6738–6782, https://doi.org/10.1021/acs.chemrev.0c00170.
[64] H.-S. Kim, J.B. Cook, H. Lin, J.S. Ko, S.H. Tolbert, V. Ozolins, B. Dunn, Oxygen vacancies enhance pseudocapacitive charge storage properties of MoO_{3-x}, Nat. Mater. 16 (2017) 454–460, https://doi.org/10.1038/nmat4810.

[65] J. Song, M.Z. Bazant, Effects of nanoparticle geometry and size distribution on diffusion impedance of battery electrodes, J. Electrochem. Soc. 160 (2013) A15–A24, https://doi.org/10.1149/2.023301jes.
[66] R.M. Vázquez, A. Mozalev, R. Calavia, F. Gispert-Guirado, X. Vilanova, H. Habazaki, E. Llobet, Gas sensing properties of the nanostructured anodic Zr–W oxide film, Sens. Actuators, B 204 (2014) 588–595, https://doi.org/10.1016/j.snb.2014.08.014.
[67] S. Mahajan, S. Jagtap, Metal-oxide semiconductors for carbon monoxide (CO) gas sensing: A review, Appl. Mater. Today 18 (2020) 100483, https://doi.org/10.1016/j.apmt.2019.100483.